JOURNAL OF GEOPHYSICAL RESEARCH, VOL. 107, NO. B3, 10.1029/2001JB000499, 2002

An *SH* hybrid method and shear velocity structures in the lowermost mantle beneath the central Pacific and South Atlantic Oceans

Lianxing Wen

Department of Geosciences, State University of New York at Stony Brook, Stony Brook, New York, USA

Received 2 March 2001; revised 7 August 2001; accepted 2 October 2001; published 29 March 2002.

[1] An *SH* hybrid method is developed for calculating synthetic seismograms involving two-dimensional localized heterogeneous structures. The hybrid method is a combination of analytic and numerical methods, with the numerical method (finite difference) applied in the heterogeneous region only and analytical methods applied outside the region. Generalized ray theory solutions from a seismic source are used to initiate the finite difference calculation, and seismic responses at the Earth's surface are obtained from the finite difference output by applying the Kirchhoff theory. We apply the hybrid method and study *SH* wave propagation near the bottom of the mantle. The shear velocity structures and the interaction of *SH* waves with these velocity structures at the base of the mantle beneath the central Pacific and South Atlantic Oceans are of particular importance. The observed *SH* waves sampling these two regions of the core-mantle boundary show very different characteristics across the epicentral distance range of 83°–108°. The *SH* waves sampling the core-mantle boundary beneath the central Pacific show a linearly increasing delay of 4 s from 98° to 108° and discernible *ScS* phases up to an epicentral distance of 102°. The *SH* waves propagating through the base of the mantle beneath the South Atlantic Ocean, on the other hand, exhibit a linearly increasing delay of 10 s from 98° to 108°, discernible multiple *ScS* phases with a same slowness as the direct *SH* waves up to 108°, and rapid variations of waveforms across small epicentral distances. Synthetic tests indicate that while the observations sampling the central Pacific can be explained by a negative shear velocity gradient of 3% (relative to the preliminary reference Earth model) at the bottom 300 km of the mantle, those sampling the South Atlantic Ocean require a 300-km-thick bottom boundary layer with a larger negative velocity gradient (up to 10%) and steeply dipping edges. The negative velocity gradient at the base of mantle beneath the South Atlantic Ocean can be best explained by partial melt driven by a compositional change produced in the early Earth's history and a vertical thermal gradient within the layer, while that beneath the central Pacific may reasonably be attributed to pure thermal effects within a thermal boundary layer. *INDEX TERMS:* 7260 Seismology: Theory and modeling; 7207 Seismology: Core and mantle; 7203 Seismology: Body wave propagation; 3210 Mathematical Geophysics: Modeling; *KEYWORDS:* Hybrid method, finite difference, wave propagation, numerical modeling, thermochemical boundary layer, D″

1. Introduction

[2] The core-mantle boundary region plays a fundamental role in mantle and core dynamics (see *Lay et al.* [1998] for a review). It is now widely recognized that there exist not only large variations of seismic velocities but also rapid transitions of seismic structures in that region. Many seismic studies indicate that the magnitudes of the seismic velocity variations may exceed 10% for P waves and perhaps 30% for shear waves near the core-mantle boundary [e.g., *Garnero et al.*, 1993; *Mori and Helmberger*, 1995; *Revenaugh and Meyer*, 1997; *Vidale and Hedlin*, 1998; *Wen and Helmberger*, 1998a, 1998b]. Some seismic observations also require two- or three-dimensional seismic structures [e.g., *Wen and Helmberger*, 1998a; *Wen et al.*, 2001]. While our ability to constrain both the geometry and the magnitude of seismic structures will bring significant progress in understanding the origin of those seismic anomalies [e.g., *Wen et al.*, 2001], the existence of three-dimensional seismic structures and their large and rapid variations of seismic properties also pose significant challenges to our modeling efforts, as trade-offs exist between geometry, magnitude, and the detailed distribution of seismic anomalies. There is an obvious demand for new techniques capable of calculating seismic responses through the strongly heterogeneous regions in the deep mantle, as well as systematic studies of interaction of seismic waves with these rapidly varying seismic structures.

[3] We have developed a two-dimensional *P-SV* hybrid method for calculating synthetic seismograms for seismic waves propagating through localized heterogeneous medium at large distances [*Wen and Helmberger*, 1998a]. Hybrid methods are combinations of numerical and analytic methods, with numerical methods applied in the heterogeneous region only. The *P-SV* hybrid method has been applied to study many seismological problems, such as the diffracted behavior of *SKS-SPdKS* phases [*Wen and Helmberger*, 1998a; *Helmberger et al.*, 1998, 2000], the precursors to *PKP* phases [*Wen and Helmberger*, 1998b; *Wen*, 2000; *Niu and Wen*, 2001], and the seismic scattering in the Earth's inner core (L. Wen and F. Niu, Seismic velocity and attenuation structures in the top of the Earth's inner core, submitted to *Journal of Geophysical Research*, 2001). We focus here on the development of an *SH*

0148-0227/02/2001JB000499$09.00

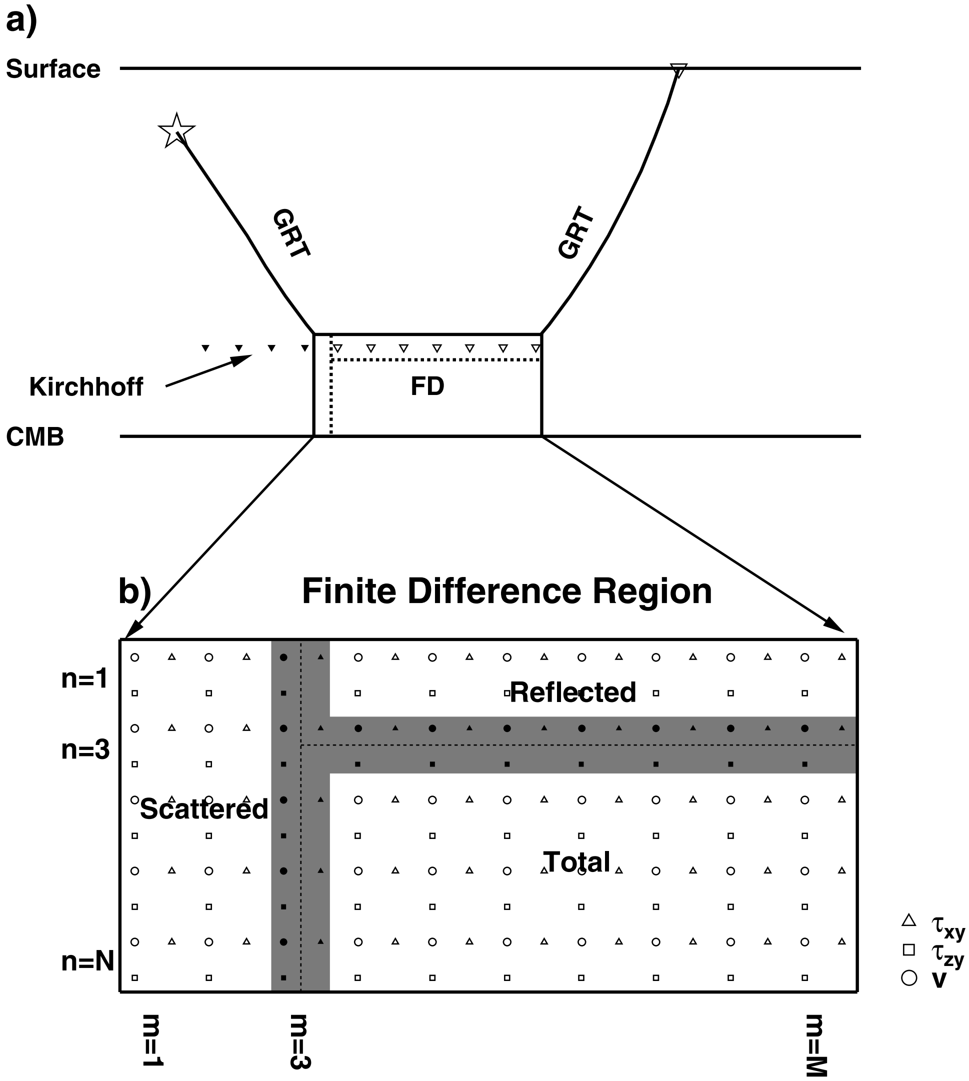

Figure 1. (a) Schematic illustration of interfacings of the hybrid method. The heterogeneous regions are assumed to be confined inside the small box, where the finite difference technique is applied. Generalized ray theory is used to calculate wave propagation from the source to the finite difference region, and synthetic seismograms at the Earth's surface are obtained by integrating convolutions of the output from the source-side along the line represented by triangles and the Green's function from the receiver to the same positions. The source-side output in positions represented by solid triangles is calculated by the generalized ray theory; that in positions represented by open triangles is obtained from the finite difference calculation. (b) Division of the finite difference region. The finite difference region is divided into three parts, where different wave fields are calculated (see text for detailed explanations).

hybrid method and a study of the interaction of *SH* waves with seismic structures near the core-mantle boundary, with particular emphasis on those beneath the central Pacific and South Atlantic Oceans. We present the theory of *SH* hybrid method in section 2, the seismic observations sampling the core-mantle boundary region beneath the central Pacific and South Atlantic Oceans in section 3, and, the study of the interaction of seismic *SH* waves with various seismic structures at the base of the mantle in section 4. We then explore seismic models appropriate for explaining the seismic data sampling the central Pacific and South Atlantic Oceans in section 5 and possible interpretations of these seismic structures in section 6.

2. A Two-Dimensional *SH* Hybrid Method Combining Generalized Ray Theory, Finite Difference, and Kirchhoff Theory

[4] The concept of the hybrid method is the same as that of *Wen and Helmberger* [1998a], except that *SH* wave propogation is considered in the present case. The *SH* wave propagation problem is illustrated in Figure 1a, where we assume the Earth flattening approximation. The heterogeneous region is bounded by a box, where a finite difference technique is applied. The generalized ray theory (GRT) solutions are interfaced with the finite difference (FD) calculation in the shaded regions in Figure 1b. The wave fields are output from the finite difference calculation in the top of the finite difference region, which are indicated by open triangles. The solutions indicated by solid triangles are calculated directly by the generalized ray theory, since those regions are affected little by the presence of heterogeneities. The synthetics at the surface of the Earth are obtained by applying the Kirchhoff method to interface the output of receivers (triangles in Figure 1a) with GRT Green's functions. Interfacings of these motions are discussed in sections 2.1 and 2.2.

2.1. GRT-FD Interfacing

[5] The staggered-grid scheme is used for finite differencing the *SH* wave equations [*Virieux*, 1984]. Finite difference grids are

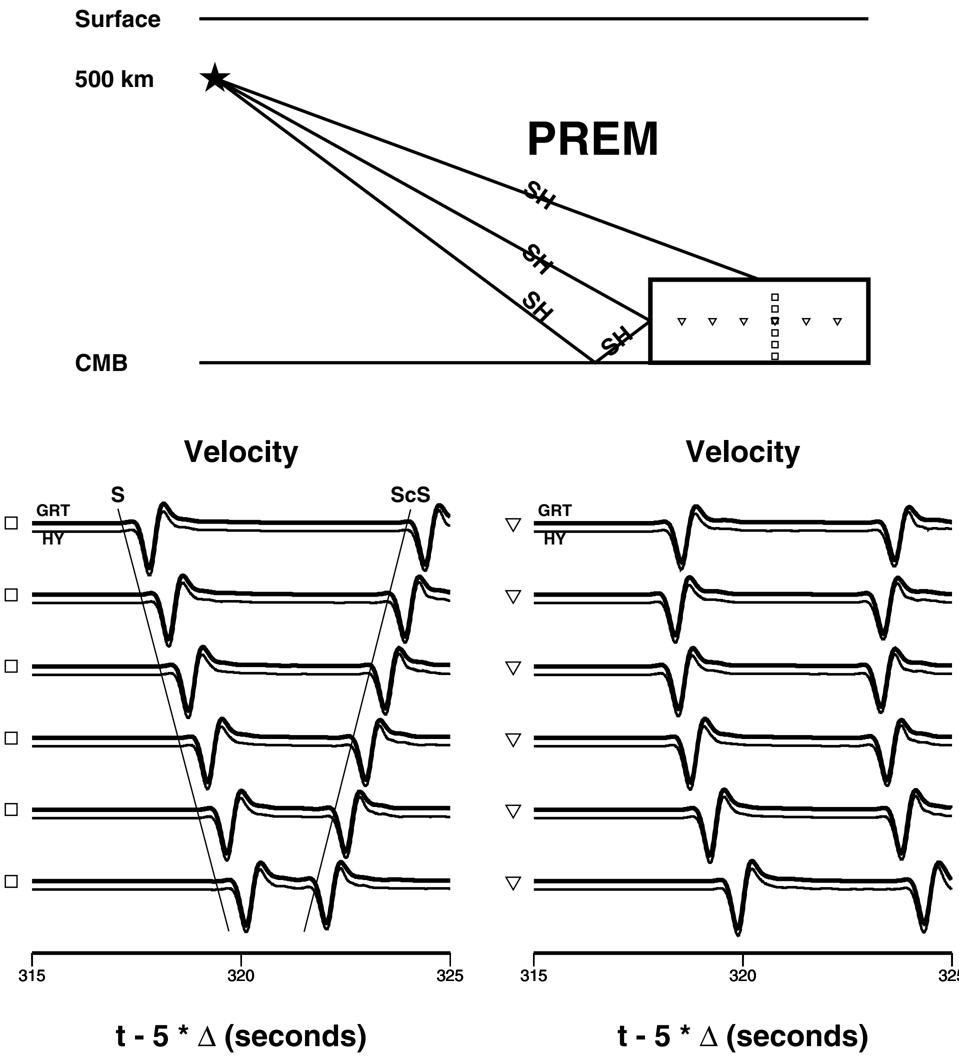

Figure 2. Comparison of tangential displacements obtained by the generalized ray theory (heavy lines) and the hybrid method (light lines) for a source depth of 500 km. The epicentral distance of the vertical cross section is 1000 km, and the separation of vertical receivers is 8 km. The separation of horizontal receivers is 55 km. PREM is used for the calculation, and the Earth-flattening approximation is applied. All seismograms are plotted to the same scale.

illustrated in Figure 1b, where tangential velocities are indicated by circles, and shear stresses are represented by triangles and squares. The finite difference grids are divided into three regions, separated by the dashed lines in Figure 1b: (1) total, where the total wave fields are calculated (the heterogeneity is only present in this region); (2) reflected, where reflected wave fields are calculated (the reflected waves are defined as the reflections from the heterogeneous region (i.e., energy propagating upward) due to the incident wave); and (3) scattered, where scattered wave fields are calculated (scattered wave fields are defined as the scattering due to the presence of the heterogeneities (i.e., energy propagating leftward)); for a one-dimensional model, these wave fields are zero.

[6] Let the incident wave field be I_0, the one-dimensional solution of the wave field be T_0, the reflected wave field due to the one-dimensional model be R_0, the total wave field be T, the reflected wave field be R, and the scattered wave field be S. I, T, R, and S are either velocity (V) or stresses (τ_{xy}, τ_{zy}). There are general relationships among S, I, T, and R, namely,

$$T = I_0 + R \text{ or } R = T - I_0,$$
$$S = T - T_0 \text{ or } T = S + T_0,$$
$$S = R - R_0 \text{ or } R = S + R_0.$$

[7] The finite difference schemes are applied directly in those regions since wave fields in those regions satisfy the wave equations individually. The explicit numerical schemes of fourth order in space and second order in time are applied in the interior of those regions, whereas those of second order in space and time [*Virieux*, 1984] are used for the grid points indicated by solid symbols in Figure 1b, where special treatments are required. For example, in order to calculate the reflected tangential velocities (V) at n = 3 (solid circles) the reflected shear stresses (τ_{zy}) at n = 3 (solid squares) are required. The shear stresses (τ_{zy}) in those positions, however, are the total wave fields as defined above. On the other hand, in order to calculate the total shear stresses (τ_{zy}) at n = 3 (solid squares) the total velocities (V) at n = 3 (solid circles) are required. The velocities V at those positions, however, are the reflected wave fields as defined above. The total velocity (V) and reflected shear stress (τ_{zy}) can be obtained by using the above three relationships between I, R, S, and T. The explicit finite difference formulations at those special regions are presented in Appendix A.

2.2. Generalized Ray Theory

[8] I_0, R_0, and T_0 can be calculated by the generalized ray theory [*Helmberger*, 1983]. With small modifications for a line source the

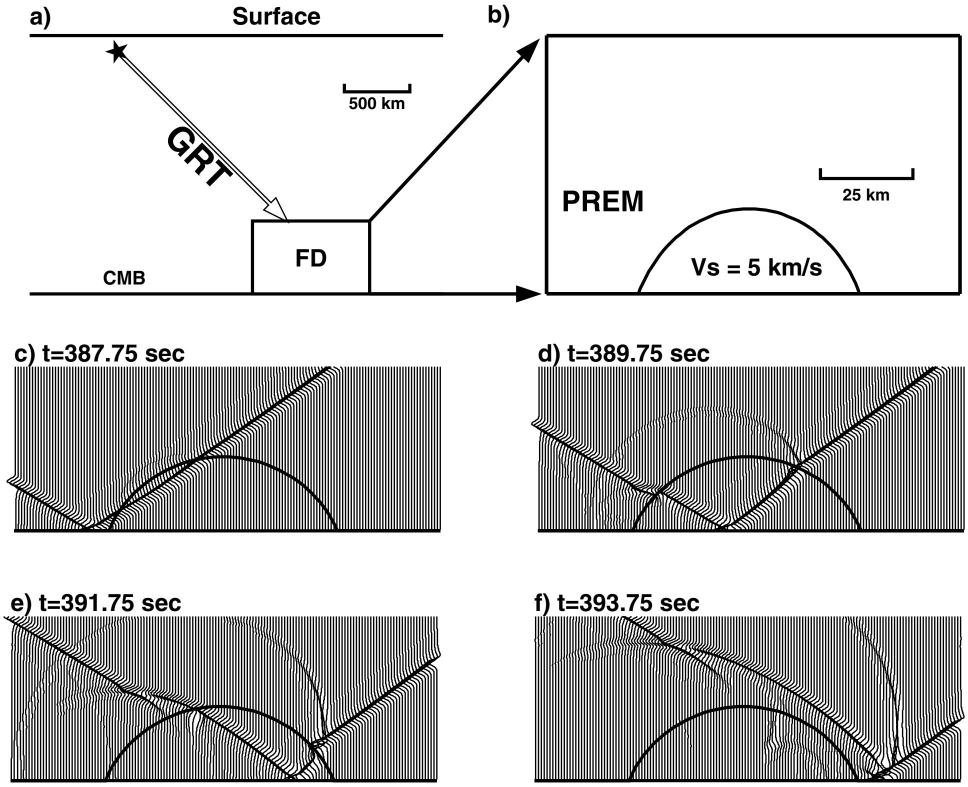

Figure 3. Snapshots of *SH* wave propagation for PREM embedded with a ridge-shaped low-velocity structure just above the core-mantle boundary. The ridge has an shear wave velocity of 5 km/s. (a and b) model setup; (c–f) snapshots of the wave fields.

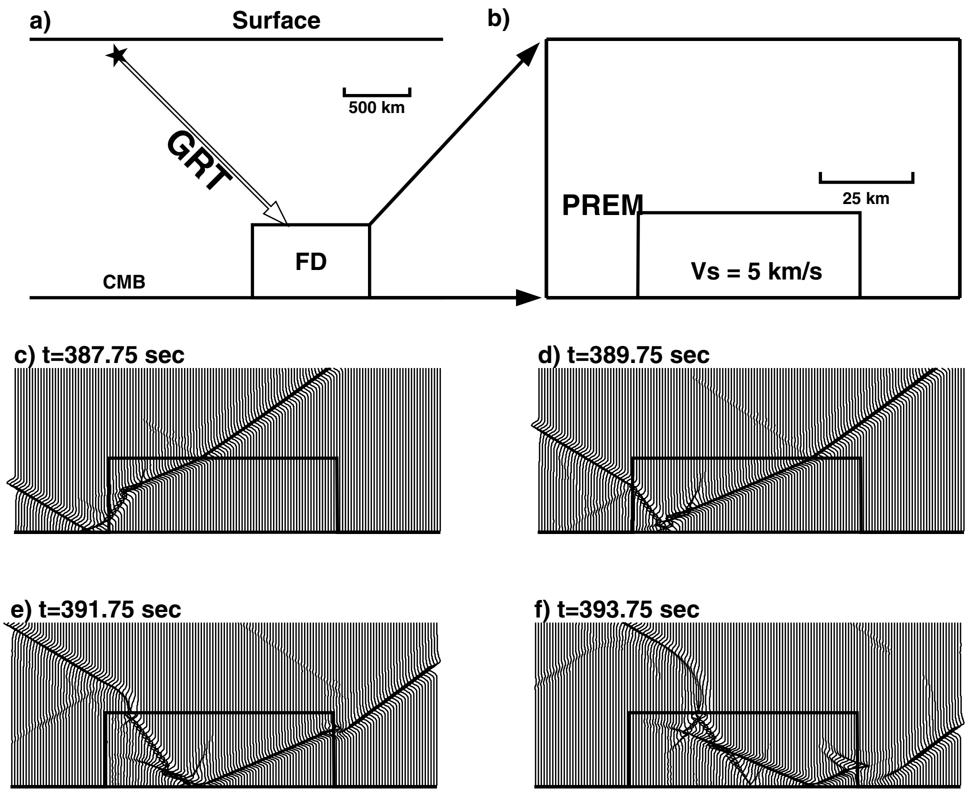

Figure 4. Same as Figure 3, except with a boxcar-shaped low-velocity region.

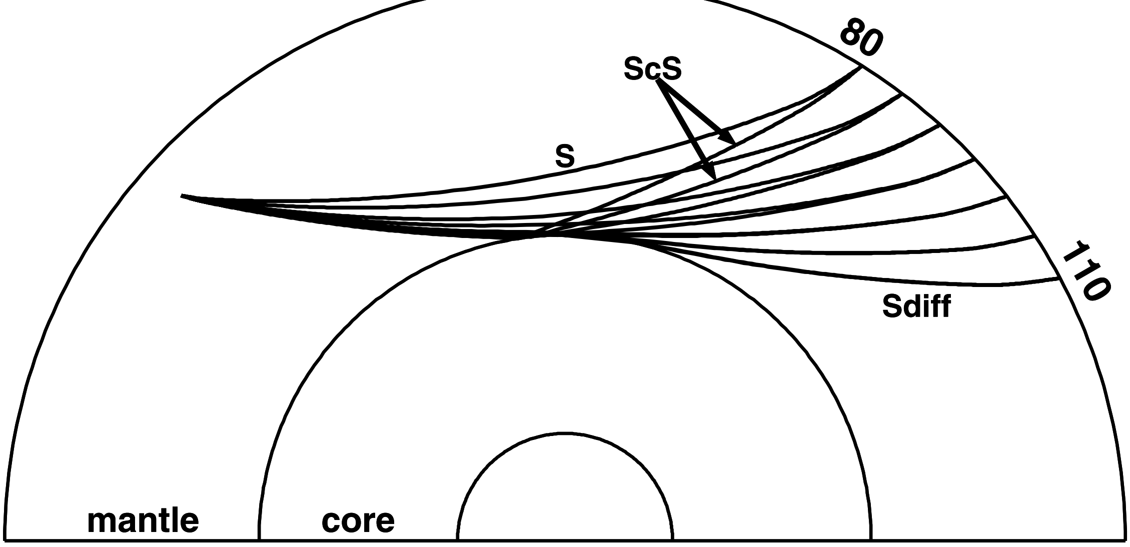

Figure 5. Ray paths of *SH*, *ScS*, and S_{diff} phases based on PREM for epicentral distances from 80° to 110°.

potentials for a receiver in a medium with a stratified velocity structure are

$$\Omega = \frac{M_0}{4\pi\rho}\left[\dot{D}(t) * \sum_{j=1}^{2} A_j SH_j V_\beta(t)\right], \quad (1)$$

where

$$V_\beta(t) = \frac{1}{\pi}\left[\sum_{i=1}^{n} \mathrm{Im}\left(\frac{1}{\eta_\beta}\Pi(p)\frac{dp}{dt}\right)_i\right],$$

p is ray parameter, ρ is density, M_0 is seismic moment, β is shear velocity, $D(t)$ is far-field time function, $\Pi(p)$ is product of the transmission and reflection coefficients, n is the number of contributing rays, and $\eta_\beta = (\beta^{-2} - p^2)^{1/2}$.

[9] The orientation constants A_j and source radiation patterns SH_j are defined by [*Helmberger*, 1983]. From the relationships between stresses and displacements,

$$\tau_{xy} = \mu(\partial V/\partial x)$$
$$\tau_{zy} = \mu(\partial V/\partial z),$$

where V is the tangential component of displacement and μ is shear modulus. Receiver functions for converting potentials to velocities and stresses are

For velocities

$$R = s^2 p;$$

For stresses

$$R_{s\tau_{xz}} = s^2\mu p^2$$
$$R_{s\tau_{yz}} = \varepsilon s^2 \mu p \eta_\beta;$$

s is the Laplace transform variable; $\varepsilon = 1$ for upgoing ray; and $\varepsilon = -1$ for downgoing ray.

[10] Tangential velocities calculated by the GRT-FD interfacing and those from GRT for an incident SH wave using the one-dimensional preliminary reference Earth model (PREM) [*Dziewonski and Anderson*, 1981] show an excellent agreement in both wave shape and absolute amplitude (Figure 2). Figure 2 (left) and Figure 2 (right) show comparisons of synthetics for receivers indicated by squares and triangles, respectively. All traces are plotted to the same scale. The first phases are direct *SH* waves (labeled S), and the second phases are the core-reflected *ScS* waves (labeled ScS).

[11] The validity of the FD technique after the GRT-FD interfacing is further demonstrated from snapshots of *SH* wave fields for models with ridge-shaped (Figure 3) and boxcar-shaped (Figure 4) low-velocity structures. The interaction of *SH* waves with the model geometry and the core-mantle boundary is clearly simulated in the finite difference calculation (Figures 3 and 4). A boxcar low-velocity structure also generates strong multiple phases inside the boxcar (Figure 4).

2.3. Kirchhoff Interfacing

[12] For any two functions, u and w, there exists a relationship

$$\int_\Gamma \left(u\frac{\partial w}{\partial n} - w\frac{\partial u}{\partial n}\right) dl = \int\int_D (u\nabla^2 w - w\nabla^2 u)\, dA, \quad (2)$$

where D is enclosed by Γ, n is outward directed normal to Γ, dl is the line integral along Γ, and dA is the areal integral in D.

[13] The wave field potential (Q) for a seismic *SH* wave propagating in a two-dimensional whole space satisfies

$$\nabla^2 Q = \frac{1}{v^2}\frac{\partial^2 Q}{\partial t^2},$$

where v is *SH* wave propagational velocity. The Laplace transform of the preceding equation over time yields

$$\left(\nabla^2 - \frac{s^2}{v^2}\right)\overline{Q} = 0.$$

The Green's function $(\overline{G})$ for a line source, by definition, satisfies

$$\left(\nabla^2 - \frac{s^2}{v^2}\right)\overline{G} = \delta(x - x')\delta(z - z'). \quad (3)$$

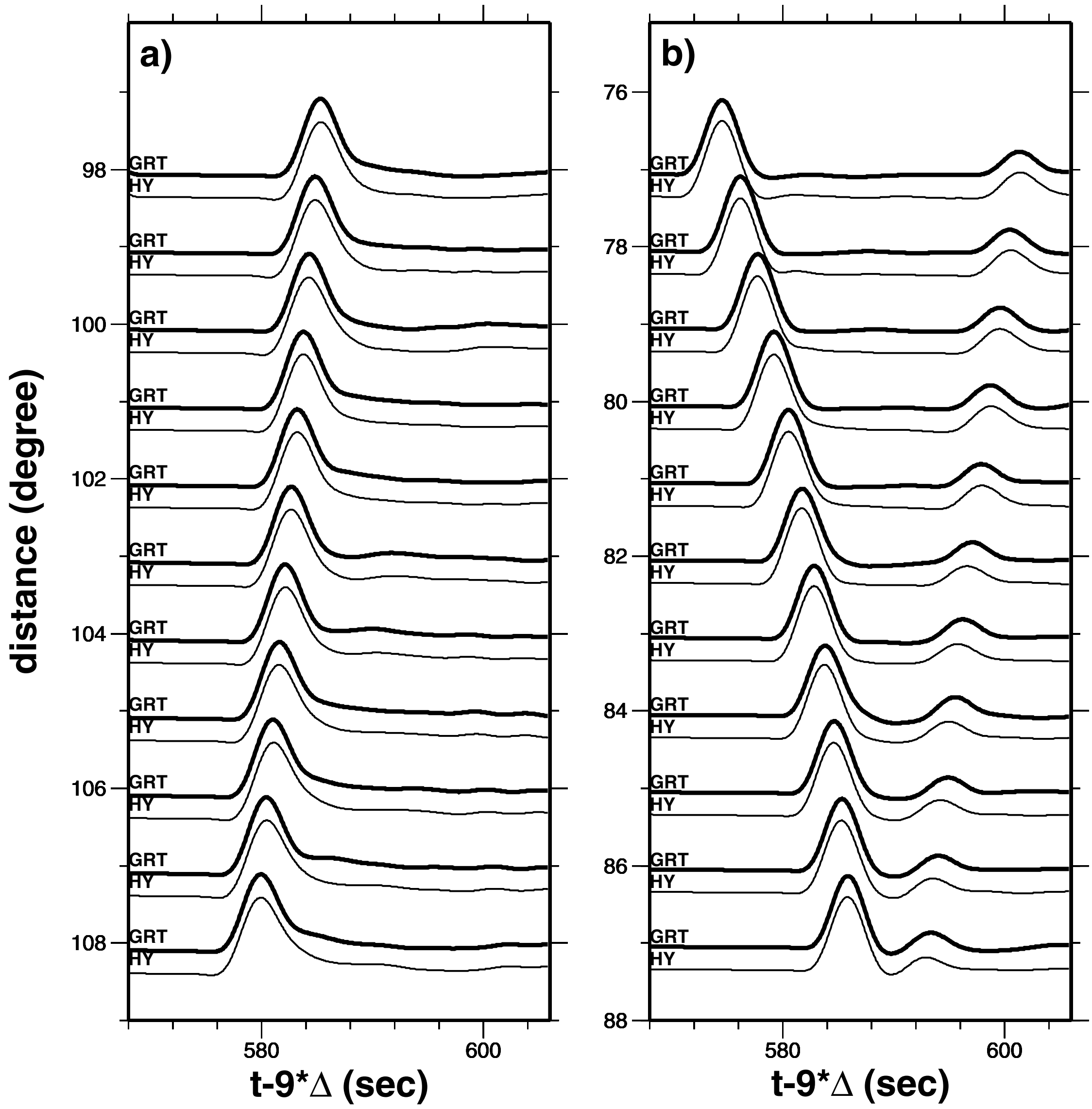

Figure 6. Comparison of *SH-ScSH* synthetics obtained by the generalized ray theory (heavy traces) and the hybrid method (light traces) based on PREM. The hybrid method synthetics are shifted away from their epicentral distances for displaying purpose. A source depth of 500 km is used in the calculation.

Inserting $\overline{G}$ and $\overline{Q}$ into (2), we have

$$\int_{\Gamma}\left(\overline{Q}\frac{\partial\overline{G}}{\partial n}-\overline{G}\frac{\partial\overline{Q}}{\partial n}\right)dl = \int\int_{D}(\overline{Q}\nabla^2\overline{G}-\overline{G}\nabla^2\overline{Q})dA = \int\int_{D}\overline{Q}\delta(x-x')\delta(z-z')dA,$$

that is,

$$\overline{Q}(x,z) = \int_{\Gamma}\left(\overline{Q}\frac{\partial\overline{G}}{\partial n}-\overline{G}\frac{\partial\overline{Q}}{\partial n}\right)dl. \quad (4)$$

[14] In this study, the integration is along a straight line just above the interface, G is calculated by GRT, and Q is the *SH* velocity output from the GRT-FD interfacing for regions indicated by open triangles in Figure 1 and from the generalized ray theory for regions indicated by solid triangles in Figure 1.

[15] The point source solution can be obtained by correcting the line source response [e.g., *Stead and Helmberger*, 1988]:

$$U_{\text{point}} = \frac{2}{\sqrt{R}+\sqrt{x}}\frac{1}{\sqrt{t}} * \frac{d}{dt}U_{\text{line}}, \quad (5)$$

where R and x are the total and horizontal distances, respectively.

[16] We check the validity of the hybrid method by comparing point source synthetics calculated by different methods for S and ScS phases at a distance range of $80°-110°$. S is the direct *SH* arrival from the source to the receiver, and *ScS* is the reflected phase from the core-mantle boundary (Figure 5). *SH* waves start to diffract along the core-mantle boundary at about an epicentral distance of 95° (Figure 5, note that the diffraction distance is both model- and source-depth-dependent). The comparison between the synthetics for a point source calculated by GRT and the hybrid method yields a good agreement (Figure 6). Both the timing and the amplitude of S and ScS phases match

Table 1. Event List

Event	Origin, UT	Latitude	Longitude	Depth, km
950823	23 Aug. 1995, 0706:03	18.86	145.19	596
970503	3 May 1997, 1646:02	−31.79	−179.38	108
970902	2 Sept. 1997, 1213:23	3.85	−75.75	199
970904	4 Sept. 1997, 0434:06	−26.57	178.34	625
971128	28 Nov. 1997, 2253:42	−13.74	−68.79	586
951006	6 Oct. 1995, 1139:36	−20.02	−175.92	209

well for synthetics calculated by the two different methods (Figure 6).

3. Seismic Observations Sampling the Central Pacific and South Atlantic Oceans

[17] We focus our detailed studies on the seismic *SH* wave propagation in the core-mantle boundary region beneath the central Pacific and South Atlantic Oceans. These two regions are devoid of surface subduction for a long period of time [*Ricard et al.*, 1993; *Wen and Anderson*, 1995]. The central Pacific is well sampled by the event-station pairs from deep earthquakes in the Fiji subduction zone to seismic stations in North America. The paths sampling the lowermost mantle beneath the South Atlantic Ocean have been significantly expanded in recent years with the deployment of several Program for Array Seismic Studies of the Continental Lithosphere (PASSCAL) seismic experiments in southern Africa. These temporary seismic networks recorded high-quality seismic data from deep events in the South American subduction zone.

[18] We select tangential displacements recorded in a PASSCAL seismic array, MOMA, in the eastern United States, the Trinet seismic network in southern California, and a few seismic stations in the Global Seismic Network, for three deep events in the Fiji subduction zone and one in the Mariana subduction zone (Table 1). The seismic data recorded for three Fiji events (951005, 970904, and 970503) sample the lowermost mantle beneath the central Pacific, and the data recorded for the Mariana event (950823) sample the core-mantle boundary region beneath the northern Pacific (Figure 7). The SH_{diff} phases show different characteristics between those sampling the lowermost mantle beneath the northern Pacific (Figure 8a) and those sampling the core-mantle boundary region beneath the central Pacific (Figure 8b). The S_{diff} phases sampling the lowermost mantle beneath the northern Pacific show simple pulse-like waveforms across the MOMA array (Figure 8a). On the other hand, the S_{diff} phases sampling the core-mantle boundary region beneath the central Pacific exhibit a discernible secondary phase up to a distance of 101.5° (phase labeled 2, Figure 8b). This secondary phase has comparable amplitudes and a smaller slowness compared to the direct *SH* waves (phase labeled 1, Figure 8b). The S_{diff} phases along both these two paths show a linearly increasing travel time delay of ∼4 s across the array, with respect to the predictions based on model IASP91. The *SH* and *ScS* phases at closer distance ranges do not show late *ScS* phases at the distance range of 90°–96° (Figure 8c). Although there is some broadening of waveform shape for recordings at the distance range between 91° and 96°, no discernible secondary phases are observed at this distance range.

[19] The seismic waves sampling the lowermost mantle beneath the South Atlantic Ocean, however, show very different characteristics for recordings both at the diffracted distance range (98°–110°) and at a closer distance range (82°–96°). At the diffracted distance range of 98°–110° (Figures 9a and 9b; recordings for event 970902 in the northern and southern parts of the array, respectively; see also Figure 7 for geographic locations sampled): (1) there is a linearly increasing travel time delay of ∼10 s across the seismic array; (2) there are clear multiple secondary phases with same move outs as the first arrivals; and (3) the waveform complexities vary

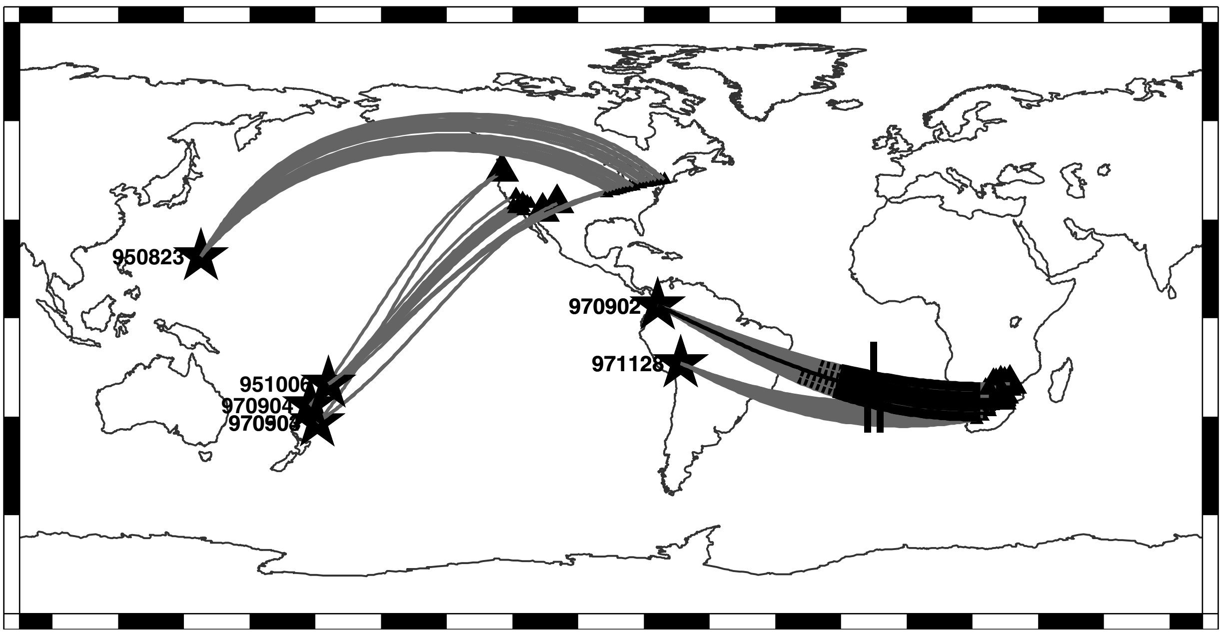

Figure 7. Great circle paths for event (star) and station (triangle) pairs used in this study (see Table 1). The *SH* waves recorded in North America for events in the Fiji subduction zone sample the core-mantle boundary region beneath the Pacific Ocean (see Figures 8a, 8b, and 8c for data), whereas those observed in southern Africa propagate through the base of the mantle beneath the South Atlantic ocean (see Figures 9a, 9b, and 9c for data). We divide the seismic observations into two groups for event 970902, with groups I and II corresponding to the northern and southern parts of the seismic array, respectively. The observations of these two groups are shown in Figure 9a (group I) and Figure 9b (group II). The dashed area indicates the transitions from the normal mantle to a 300-km-thick layer (solid area) with shear velocity reductions linearly decreasing from 2% (top) to 10–12% (bottom).

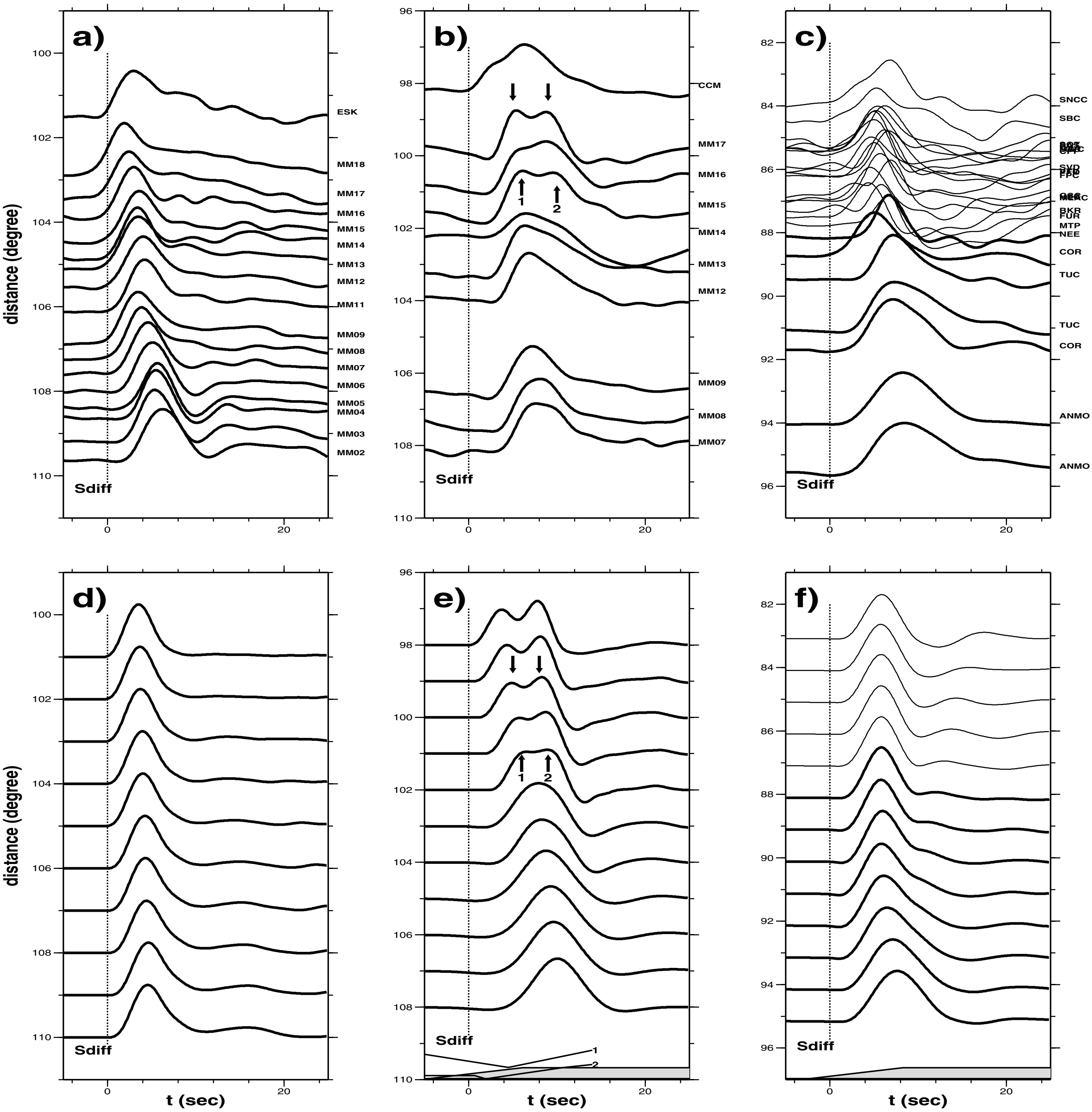

Figure 8. (a–c) Observed tangential displacements sampling the Pacific and (d–f) synthetics and seismic models for explaining these observations for Figures 8a, 8b, and 8c, respectively. The central Pacific is sampled by the seismic data recorded in North America for events occurring in the Fiji subduction zone (Figure 7 and Table 1). Figures 8a and 8b are for the tangential displacements recorded for events 950823 and 951006 (Figure 7), respectively. Figure 8c is a collection of the tangential displacements for events 970904 and 970503. The observations sampling the northern Pacific (Figure 8a) are explained by PREM (Figure 8d). The observations sampling the central Pacific (Figures 8b and 8c) are explained by a model with a negative velocity gradient of 3% at the bottom 300 km of the mantle with a shallowly dipping geometry (Figures 8e and 8f). Several phases are labeled in the data and are explained in synthetics, with their ray paths schematically plotted at the bottom of Figure 8e. Each trace is self-normalized and aligned according to the theoretical predicted direct arrivals (t = 0), based on the IASP91 model.

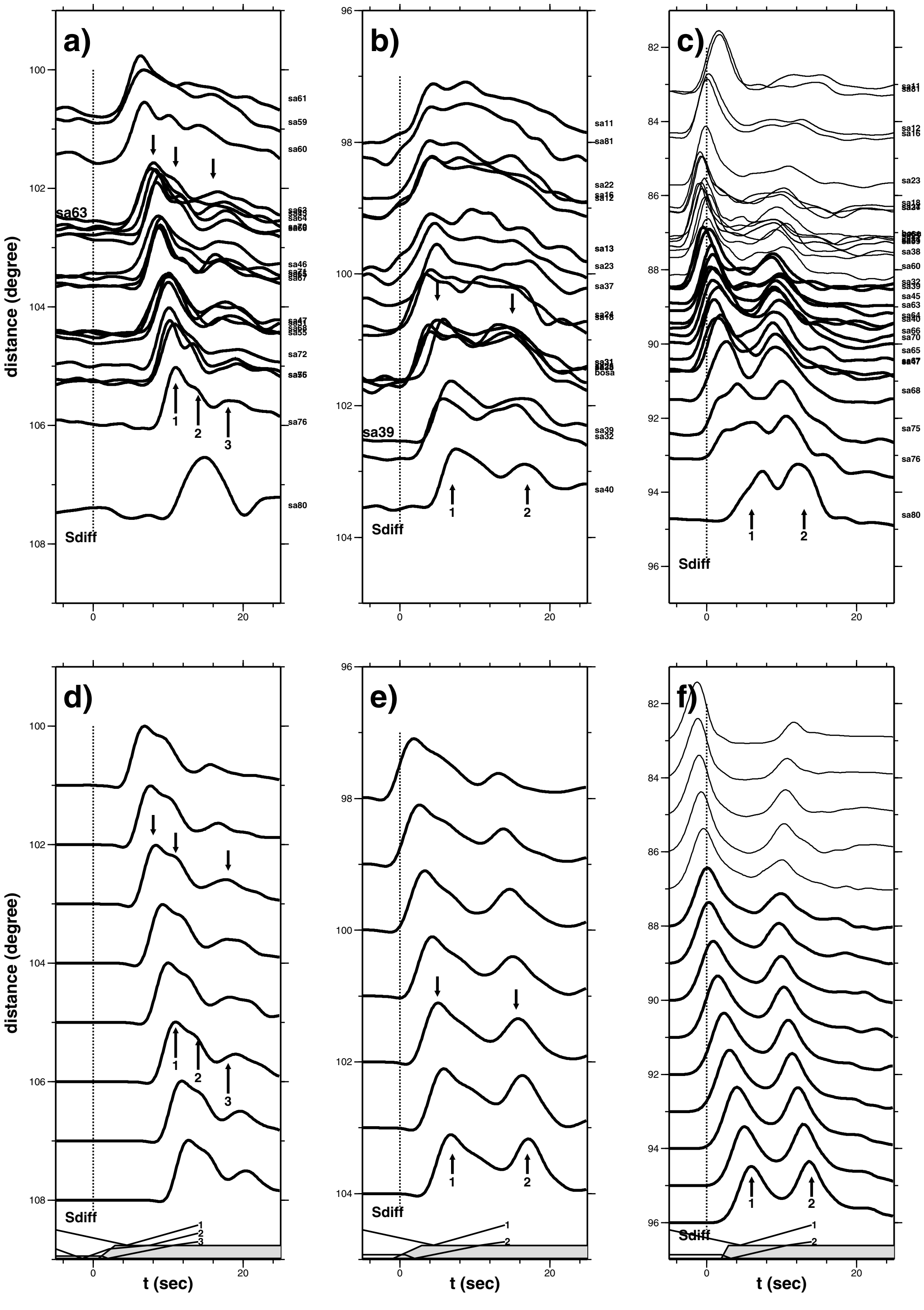

Figure 9. (a–c) Observed tangential displacements sampling the South Atlantic Ocean and (d–e) synthetics and seismic models for explaining these observed displacements for Figures 9a, 9b, and 9c, respectively. The South Atlantic Ocean is sampled by the recordings in the Kaapvaal seismic array in southern Africa for events occurring in the South American subduction zone (Figure 7 and Table 1). Figures 9a and 9b show the tangential displacements recorded for event 970902 (Figure 7) in the northern (paths labeled I in Figure 7) and southern (paths labeled II in Figure 7) parts of the Kaapvaal seismic array, respectively. Figure 9c shows the displacements recorded for event 971128. These observations are explained by models with a negative velocity gradient linearly varying from 2% (top) to 12% (bottom) at the bottom 300 km of the mantle and steeply dipping edges (Figures 9d–9f). Several phases are labeled in the data and are explained in synthetics (Figures 9d–9f) with these ray paths schematically plotted at the bottom of each panel. Each trace is self-normalized and aligned according to the theoretical predicted direct arrivals (t = 0), based on the IASP91 model.

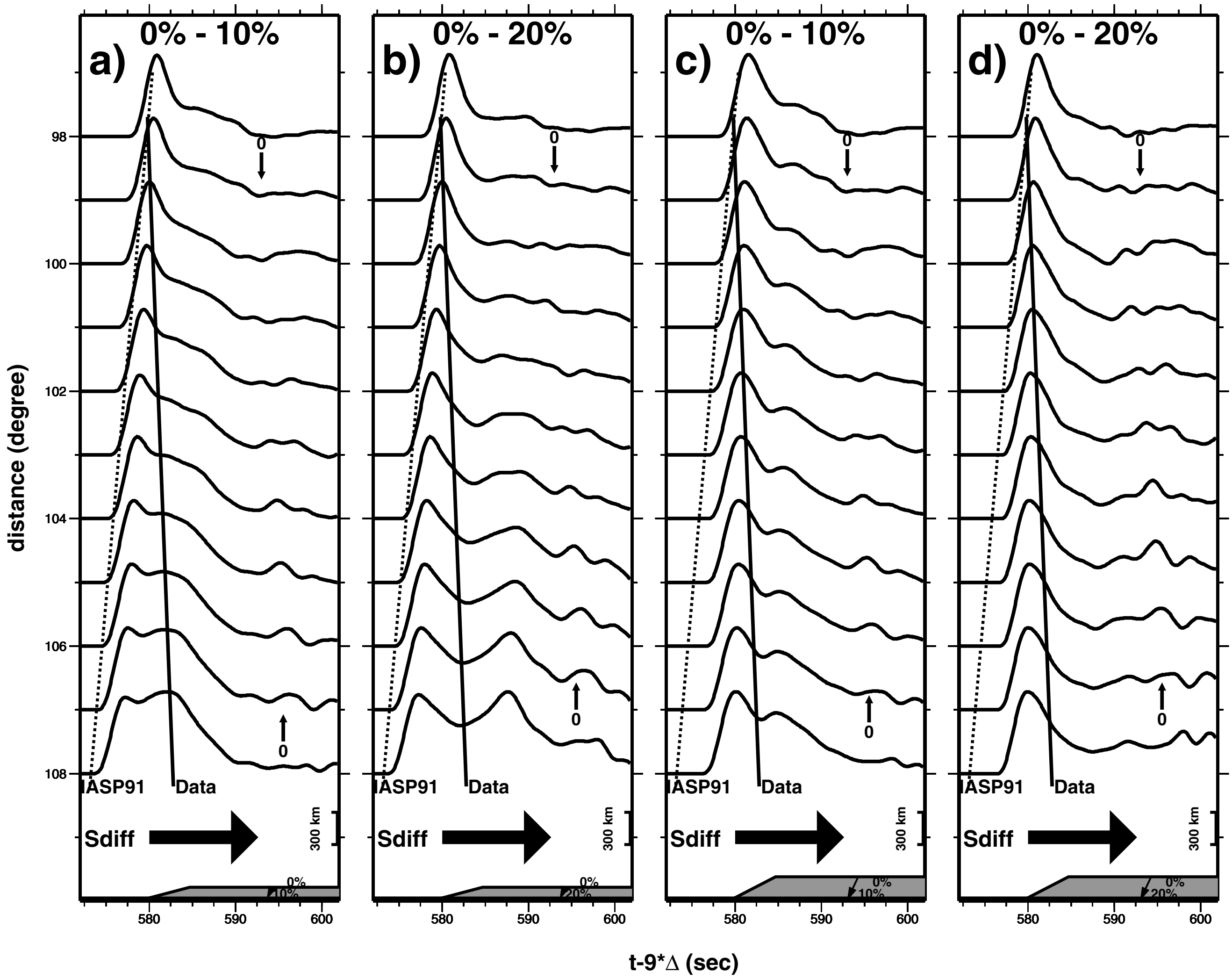

Figure 10. Synthetics calculated using models with thicknesses of (a and b) 100 km and (c and d) 200 km and negative shear velocity gradients of 10% (Figures 10a and 10c) and 20% (Figures 10b and 10d) at the base of the mantle. The dashed lines indicate the predicted arrivals based on the IASP91 model, and the heavy lines indicate the first arrivals observed in event 970902. Note that the same travel time delays are predicted for models with a same thickness, regardless of the magnitude of the negative velocity gradient. The geometries of the boundary layer are illustrated at the bottom of each panel. There are no lateral velocity gradients within the model wedges. The phase labeled as 0 is a truncation phase of the hybrid method calculation.

rapidly across small epicentral distances. The closest station separation between the northern and southern parts of the array is 113 km (Figure 7). Note that the waveform complexities are markedly different between the two group of observations (Figures 9a and 9b). At a closer distance range of 82°–96° (Figure 9c; recordings for event 971128; see also Figure 7 for geographic locations sampled): (1) there is a change of travel time behaviors for the recordings across the seismic array, with seismic waves bottoming 300 km above the core-mantle boundary showing no relative travel time delays across the array (light traces) and those bottoming lowermost 300 km of the mantle exhibiting a linearly increasing travel time delay of ~5 s across the array (heavy traces), and (2) the *ScS* phases show large time separations from the direct waves and a rapid increase of relative amplitude from 83° to 95°.

[20] These travel time delays and waveform complexities cannot be caused by mislocation of the earthquake and the seismic heterogeneities in the source-side mantle. Mislocation of an earthquake and the effects of the source-side mantle heterogeneities would result in a uniform travel time delay and similar waveform complexities across the seismic array, as these seismic waves propagate along almost identical ray paths in the source-side mantle. Take two waveforms recorded at stations sa63 (Figure 9a) and sa39 (Figure 9b); for example, phase 2 observed at sa63 does not exist in the recording at sa39 and phase 3 observed at sa63 is different from phase 2 observed at sa39 (Figures 9a and 9b). Here are geographic separations of their ray paths in the mantle:

Depth	Separation
source-side 410km	0.03°
source-side 670 km	0.08
source-side CMB	1.72°
receiver-side CMB	1.83°

The source-side seismic heterogeneities in the transition zone region would unlikely generate different waveform complexities between the two recordings, as they have a period of ~3 s, but propagate within a distance range of 0.03°–0.08° in the source-side transition zone.

[21] The waveform complexities cannot be a result of a complicated earthquake source for two reasons: (1) the waveform complexities in the two groups are markedly different and (2) the

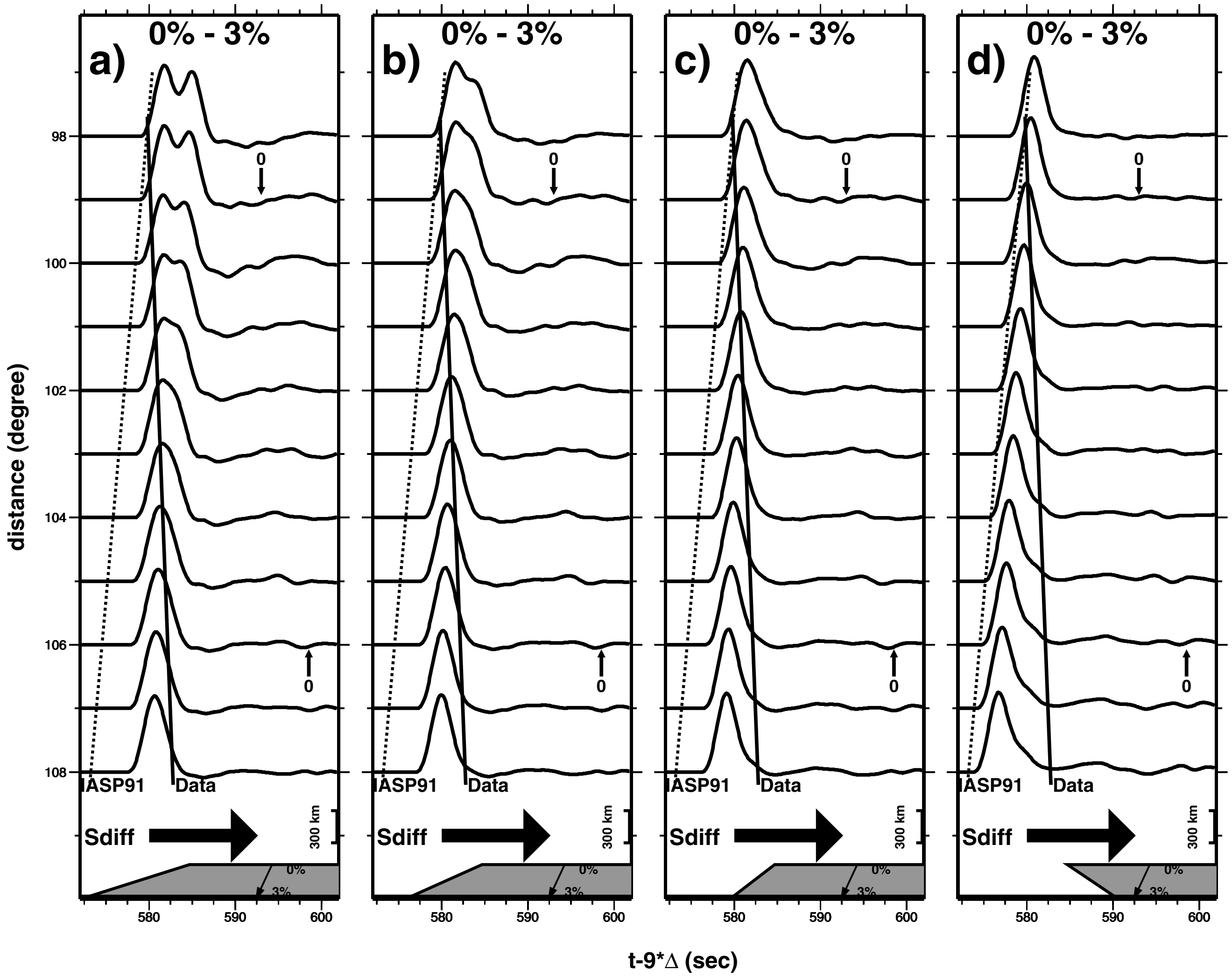

Figure 11. Examples of synthetics calculated using 300-km-thick models with a background negative velocity gradient of 3% with various geometries. The dashed lines indicate the predicted arrivals based on the IASP91 model, and the heavy lines indicate the first arrivals observed in event 970902. The geometries of the boundary layer are illustrated at the bottom of each panel. Note that *ScS* phases are visible up to an epicentral distance of 102° with a different slowness from that of the direct arrivals (Figure 11a). There are no lateral velocity gradients within the model wedges. The phase labeled as 0 is a truncation phase of the hybrid method calculation.

waveform observed at another station at a similar epicentral distance which samples a different path through the mantle displays a simple pulse-like shape, indicating a simple source time function [*Wen et al.*, 2001]. Near-station effects and the upper mantle structure beneath Africa appear to contribute little to the observed time delays across the seismic array because recordings for an earthquake at a closer distance range show little time variation across the seismic array [*Wen et al.*, 2001]. The complexities and large time delays are not caused by seismic structures in the mid-lower mantle beneath Africa either since the *SH* phases bottoming more than 300 km above the core-mantle boundary from event 971128 (Figure 9c, light traces) exhibit simple waveforms and little residual time variations across the array. These phases and the direct SH_{diff} phases in event 970902 sample a similar receiver-side mid-lower mantle. Moreover, the observations from other event-station pairs from the South Atlantic Ocean and the south Sandwich Islands to the European-Mediterranean area, which sample the same core-mantle boundary region but different parts of the mid-lower mantle, show exactly the same travel time behaviors for the *S*, S_{diff} phases as those recorded in southern Africa [*Wen et al.*, 2001], confirming that both the travel time delays and the waveform complexities observed in the southern African array are caused by anomalous seismic structures in the lowermost 300 km of the mantle. Finally, there is little travel time difference between SH_{diff} and SV_{diff} phases for this event, suggesting that most of the effects are caused by isotropic variations of seismic velocity. This is consistent with the anisotropy study in this region [*Fouch et al.*, 1999]. In section 4 we focus on detailed studies of the interaction of seismic *SH* waves with seismic structures in the lowermost 300 km of the mantle. It will also become clear that both the linearly increasing travel time delay and waveform complexities observed in the southern African array can only be explained by models with large shear velocity reductions in the lowermost 300 km of the mantle, corroborated well by all the seismic observations we discuss above.

4. *SH* Wave Propagation Through a Low-Velocity Bottom Boundary Layer

[22] We have explored several hundred models for studying the seismic velocity structures and the interaction of *SH* waves with

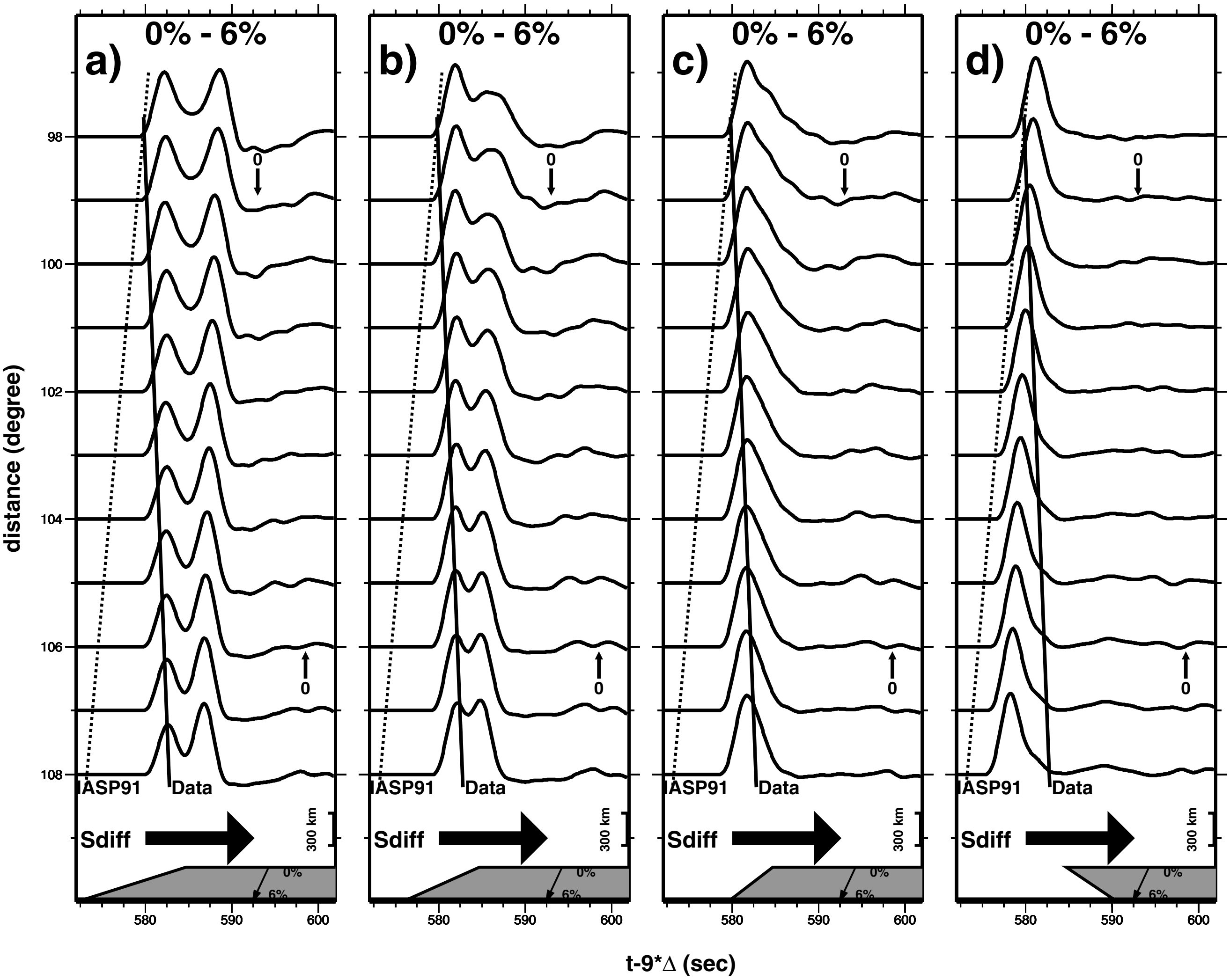

Figure 12. Same as Figure 11, except that the background negative velocity gradient is 6%. Note that strong *ScS* phases are observed, with a slowness approaching that of the direct arrivals, in the whole distance range of 98°–108°.

these velocity structures at the base of the mantle. We present some examples of synthetic seismograms to gain some insights into the interaction of seismic *SH* waves with seismic structures at the base of the mantle. The effects of a negative velocity gradient at the base of the mantle and its geometry on the seismic travel times, waveforms, and variations of waveform complexities across a small epicentral distance are of particular importance. We focus on the *SH* wave propagation at the diffracted distance range of 98°–108° first, as seismic waveforms at this distance range are sensitive to both the radial velocity gradient and the geometry of the seismic structures in the bottom of the mantle. We also discuss trade-offs between the magnitude of seismic velocity reduction and the geometry in predicting seismic responses at the distance range of 83°–95°.

[23] The only plausible way to generate a linearly increasing travel time delay of 10 s across the distance range of 98°–108° is that seismic *SH* waves encounter a 300-km-thick layer with large negative shear velocity reductions at the base of the mantle. The magnitude of the travel time delay requires such large velocity reductions in the bottom of the mantle that the direct seismic waves would propagate along the top of the low-velocity anomaly. In this case, the travel time delay is controlled by the thickness, rather than the velocity reductions, of the bottom boundary layer. Models with a smaller thickness cannot produce a linearly increasing travel time delay of 10 s, regardless of the velocity reductions inside the layer (e.g., Figure 10).

[24] A negative shear velocity gradient of 3% across the bottom 300 km of the mantle produces a linearly increasing travel time delay of 4 s at the distance range of 98°–108° (Figure 11). Depending on the geometry of the seismic structure, *ScS* phases are sometimes visible up to an epicentral distance of 102°. These *ScS* phases have a smaller slowness than that of the direct arrivals (Figures 11a and 11b). Both the relative amplitude and timing between the *ScS* phases and the direct arrivals and the termination distance of the *ScS* phases strongly depend on the geometry of the seismic structures. A shallower edge dip generates synthetics with a larger *ScS* termination distance, a longer *ScS*-*S* time separation, and a stronger relative *ScS* amplitude (Figures 11a, 11b, and 11c). Models with an inward dipping geometry produce simple waveforms and a smaller linearly increasing travel time delay (Figure 11d).

[25] An increase of the negative velocity gradient to 6% at the bottom of the mantle produces several noticeable effects on synthetics (Figure 12): (1) the *ScS* phases have a more similar slowness to the direct arrivals; (2) strong *ScS* phases are visible throughout the whole distance range of 98°–108°; and (3) both the travel time delays and the relative *ScS* amplitudes increase in the synthetics. Qualitatively, we see similar effects of changing model

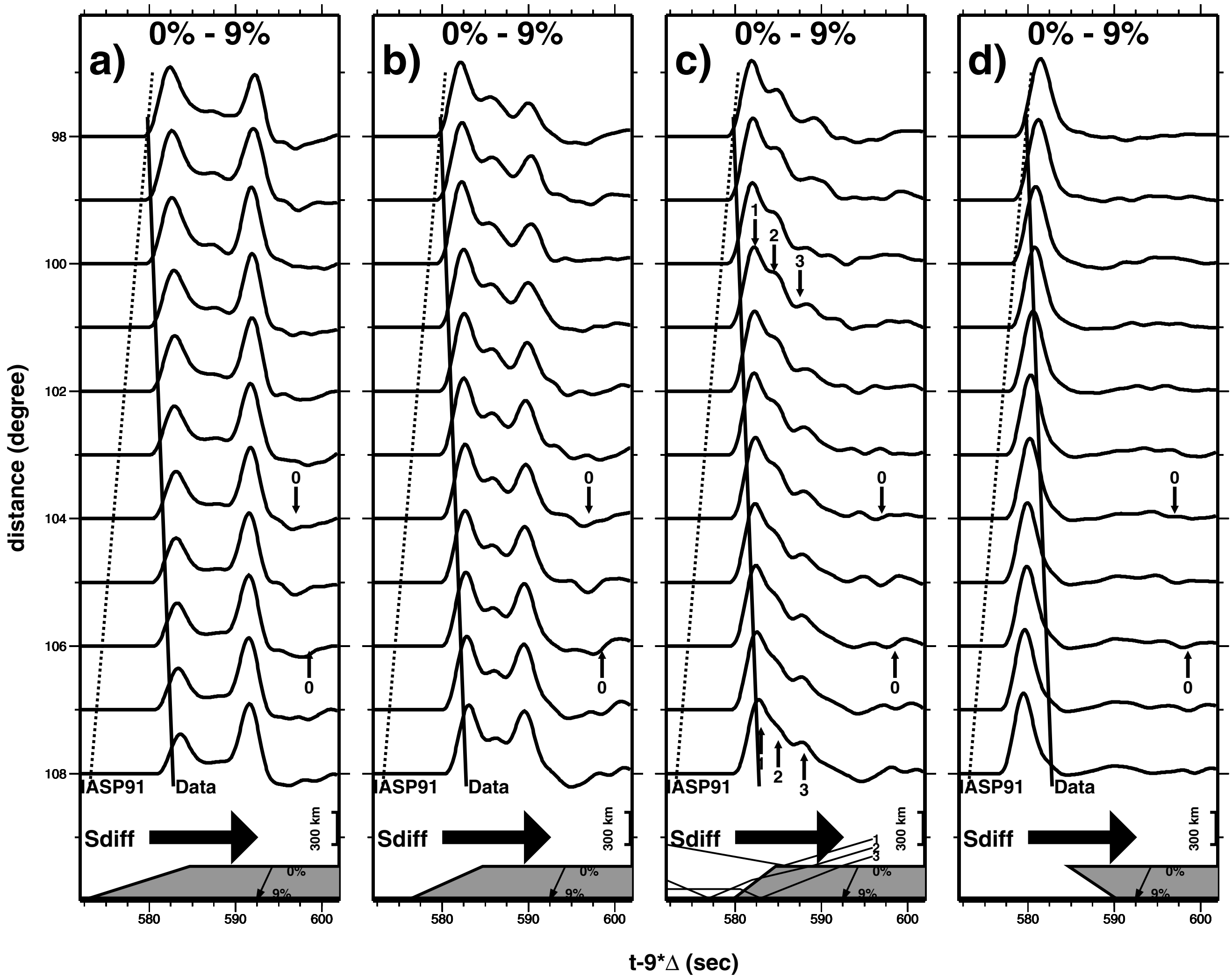

Figure 13. Same as Figure 11, except that the background negative velocity gradient is 9%. Note that an additional *ScS* phase starts to emerge for models with a steeply dipping edge (Figures 13b and 13c). The ray paths of three phases labeled in the synthetics in Figure 13c are schematically plotted in the bottom. Note also the travel time delays predicted by the models with this large negative velocity gradient.

geometry on synthetics as in Figure 11. A shallower edge dip generates synthetics with a longer *ScS-S* time separation and a stronger relative ScS amplitude (Figures 12a, 12b, and 12c). Models with an inward dipping geometry still produce simple waveforms and a smaller linearly increasing travel time delay (Figure 12d).

[26] Several characteristics begin to emerge in the synthetics for models with a strong negative shear velocity gradient of 9% at the bottom of the mantle (Figure 13): (1) The predicted linearly increasing travel time delay approaches ~8 s (Figures 13a, 13b, and 13c); (2) there appears an additional ScS phase for models with steeply dipping edges (phases labeled 2, Figure 13c); (3) these multiple *ScS* phases have almost the same move outs as the direct arrivals; and (4) synthetic waveforms are sensitive to small angle variation of edge dip (Figures 13b and 13c). All these characteristics resemble what are observed in the seismic data sampling the South Atlantic Ocean (Figures 9a and 9b). A large linearly increasing travel time delay is generated because the direct seismic waves diffract along the top of the low-velocity layer due to the presence of the strong negative velocity gradient. The additional *ScS* phase is a triplication of the reflected phase off the core-mantle boundary outside the boundary layer (see paths in the bottom of Figure 13c). Both the triplicated phases and the waveform sensitivity to the small angle variation of the edge dip are the consequences of the strong negative velocity gradient. They independently place a bound on the minimal negative velocity gradient at the base of the mantle.

[27] Although a negative velocity gradient of 12% produces qualitatively similar waveform characteristics as a negative velocity gradient of 9% (Figure 14), the details of their waveform features make these two types of models resolvable. There exist trade-offs between the magnitude of the negative velocity gradient and the angle of the edge dip in predicting the time separation between the *ScS* phase and the direct arrival (e.g., Figures 13a and 14b). However, different velocity gradients also predict different relative *ScS* amplitudes (e.g., Figures 13a and 14b). The existence of the triplicated phase and the relative timing and amplitude among different phases are sensitive to both the magnitude of the negative velocity gradient and the geometry of the seismic structures (see Figures 13c and 14c).

[28] The waveform features and their rapid variations observed in the above synthetics are unique consequences of strong negative velocity gradients at the base of the mantle.

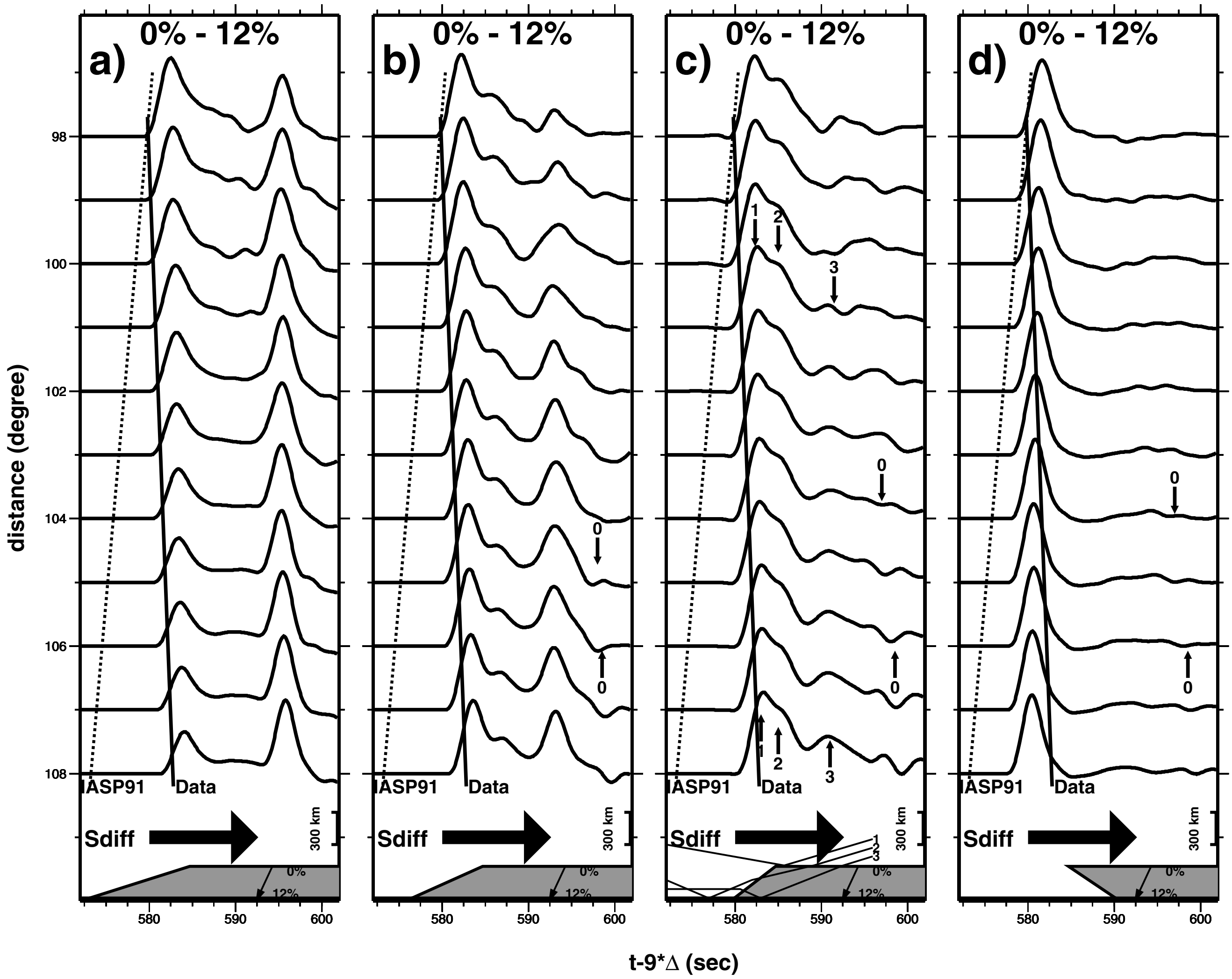

Figure 14. Same as Figure 13, except that the background negative velocity gradient is 12%. Note different relative timings and amplitudes among three phases compared to those for the models with a negative velocity gradient of 9% (compare Figures 13c and 14c).

Models with ultralow-velocity zones embedded within a small negative velocity gradient (1–3%) produce seismic responses different from those observed for the simple models with strong negative velocity gradients (e.g., Figures 13 and 14) in several aspects (Figure 15): (1) they can only produce a linearly increasing travel time delay of ~5 s; (2) they produce *ScS* phases with a different slowness from the direct waves; (3) they cannot produce a triplicated phase; (4) they generate very complicated waveforms with many multiples inside the layer and pulse-like direct arrivals (Figure 15), different from the waveform characteristics observed in the seismic data (Figures 9a and 9b) and the synthetics calculated using models with strong negative velocity gradients (e.g., Figures 13a, 13b, 13c, 14a, 14b, and 14c).

[29] The multipathed *ScS* phases observed in some synthetics (e.g., labeled as 2, Figure 14c) also independently require a certain thickness of the negative velocity layer. It is clear from their ray paths (e.g., Figure 14c) that a thin layer would not allow the multipathed *ScS* phase to separate from the direct waves. Synthetics tests indicate that at this particular distance range a thickness of at least 250 km is required so that the triplicated *ScS* phases produced by the strong negative velocity gradient and the steeply dipping edges could sufficiently separate from the direct arrivals (Figure 16). Note also that the predicted travel time delay is also smaller than those predicted with 300-km-thick layers (see Figure 14).

[30] At a closer distance range of 83°–95°, however, trade-offs exist between the magnitude of seismic velocity reduction and the geometry of seismic structure for predicting some features of seismic responses, especially the differential travel times between *S* and *ScS* phases. A model with a strong negative velocity gradient and a steeply dipping edge could produce the same differential *ScS-S* travel times as a model with a smaller negative velocity gradient and a more shallowly dipping edge (e.g., Figure 17). The relative *ScS* amplitudes across the distance range might still be used to resolve the magnitude of the negative velocity gradient, as a stronger negative velocity predicts a more rapid increase of relative *ScS* amplitude from 83° to 95° (e.g., Figure 17). We should, however, point out that caution is required to use relative *ScS* amplitude as an additional constraint to the velocity structures, as the relative *ScS* amplitudes at this distance range would also be affected by uncertainties in earthquake radiation pattern and seismic structures elsewhere (Figure 5).

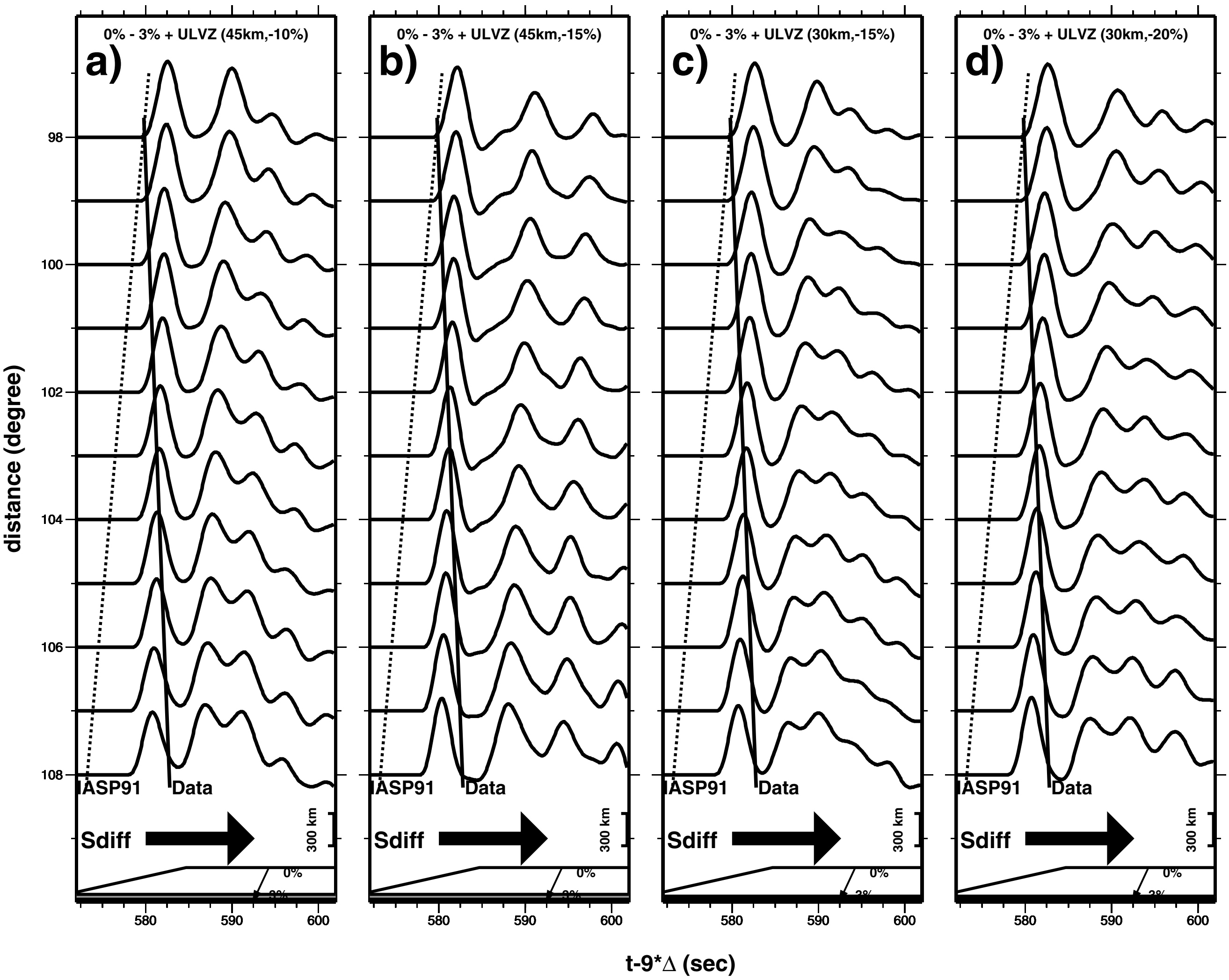

Figure 15. Examples of synthetics calculated using 300-km-thick models with a background negative velocity gradient of 3% embedded with ultralow-velocity zones at the core-mantle boundary with (a) a thickness of 45 km and a shear velocity reduction of 10%, (b) a thickness of 45 km and a shear velocity reduction of 15%, (c) a thickness of 30 km and a shear velocity reduction of 15%, and (d) a thickness of 30 km and a shear velocity reduction of 20%. The dashed lines indicate the predicted arrivals based on model IASP91, and the heavy lines indicate the first arrivals observed in event 970902. The geometries of the boundary layer are illustrated at the bottom of each panel.

5. Seismic Models in the Lowermost Mantle Beneath the Central Pacific and South Atlantic Oceans

[31] The observed travel time delays and waveform features can be used to constrain seismic structures beneath the central Pacific and South Atlantic Oceans at the bottom of the mantle. The rapid variations of waveform complexity across small epicentral distances observed in the southern African seismic array also provide an additional constraint to the seismic models beneath the South Atlantic Ocean.

[32] The observed travel times and waveforms for the *SH* waves sampling the central Pacific (Figures 8b and 8c) suggest models with a small negative velocity gradient at the base of the mantle. Indeed, the observed slowness of the *ScS* phases and their disappearance at large distance (Figure 8b) can be explained by a model with a negative velocity gradient of 3% at the bottom 300 km of the mantle (Figure 8e). A negative velocity gradient of 3% also explains the observations sampling the central Pacific at closer distances (Figures 8c and 8f). Our results are consistent with previous studies [*Ritsema et al.*, 1997; *Wysession et al.*, 1999]. The observed *SH* waveforms sampling the northern Pacific (Figure 8a) can be reasonably explained by PREM (Figure 8d).

[33] The characteristics of the observed tangential displacements sampling the South Atlantic Ocean, on the other hand, suggest the existence of a strong negative velocity gradient (>9%) at the bottom 300 km of the mantle. There are several independent lines of evidence indicating a change of velocity structure at 300 km above the core-mantle boundary and the existence of a strong negative velocity gradient at the base of the mantle beneath the South Atlantic Ocean:

1. There is a change of travel time behavior for the seismic waves observed in event 971128, with little travel time delay for seismic waves bottoming 300 km above the core-mantle boundary and a linearly increasing travel time delay for seismic waves turning within the bottom 300 km of the mantle (Figure 9c). The exactly same change of travel time behaviors is also observed from other event-station pairs sampling the same regions of the core-mantle boundary but different parts of the mid-lower mantle [*Wen et al.*, 2001].

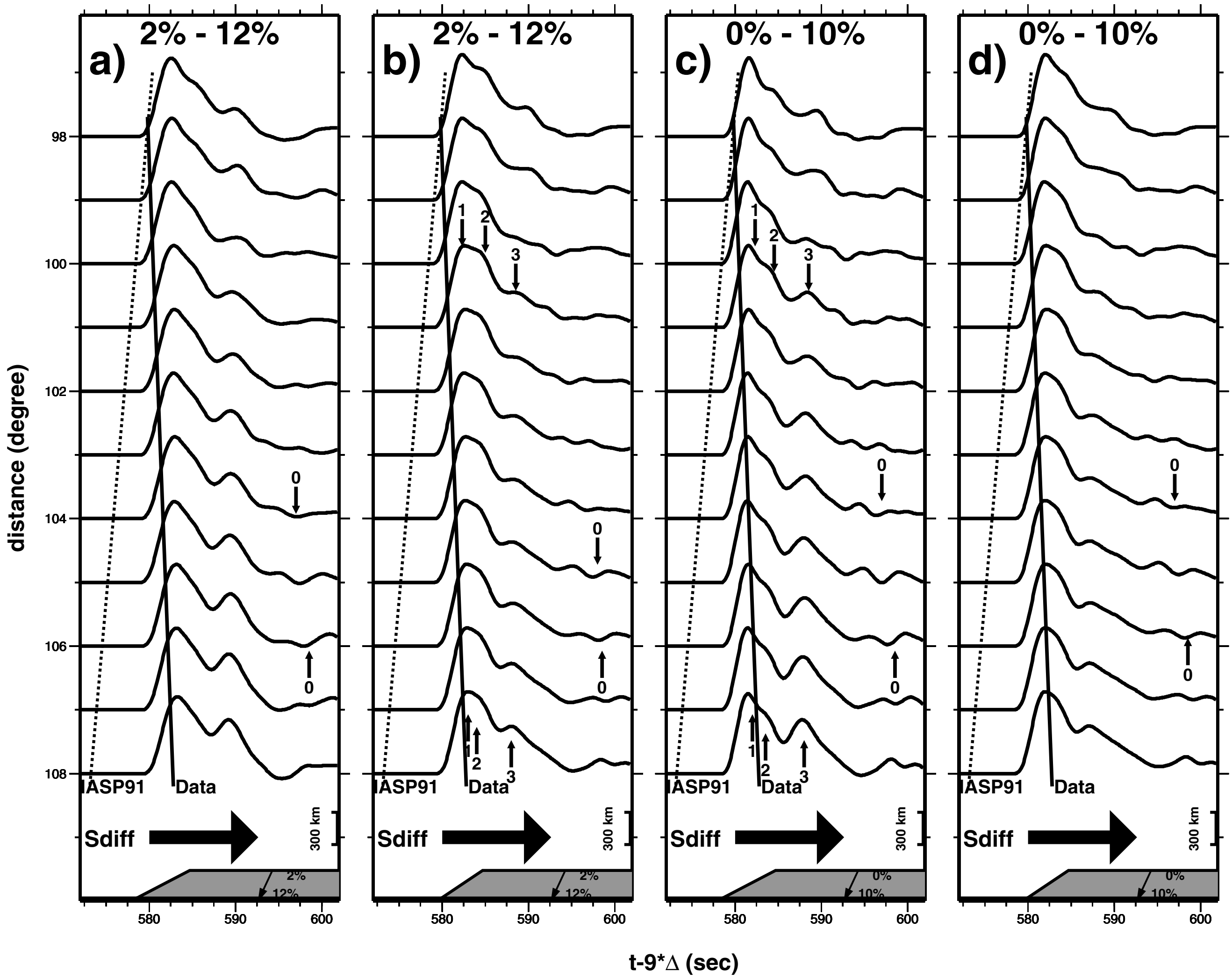

Figure 16. Examples of synthetics calculated using 250-km-thick models with strong negative velocity gradients and various geometries. The dashed lines indicate the predicted arrivals based on the IASP91 model, and the heavy lines indicate the first arrivals observed in event 970902. The geometries of the boundary layer are illustrated at the bottom of each panel. The negative velocity gradients are from 2% (top) to 12% (bottom) (Figures 16a and 16b) and from 0% (top) to 10% (bottom) (Figures 16c and 16d). Note that the multipathed phases (labeled as 2) are barely recognizable in the synthetics.

2. The only plausible model to explain a linearly increasing travel time delay of 10 s observed across the distance range of 98°–108° (Figure 9a) is a 300-km-thick bottom boundary layer with strong negative velocity reductions (e.g., Figure 10).

3. The observed existence of the triplicated phases (labeled 2, Figure 9a) requires a boundary layer with strong velocity gradients and a thickness of at least 250 km.

4. The observed identical move outs of the multiple *ScS* phases to that of the direct arrivals suggest a large negative velocity gradient.

5. The observed rapid variations of waveform across small epicentral distances (Figures 9a and 9b) require models producing synthetics sensitive to a small change of model parameters. This sensitivity can be easily accomplished when the bottom boundary layer has a strong negative velocity gradient (e.g., Figure 14).

6. Although there exist trade-offs between magnitude of the negative velocity gradient and model geometry in explaining the differential travel times between *ScS* and *S* phases at the distance range of 83°–95° (Figure 17), the rapid increase of *ScS* relative amplitudes observed in the seismic data at this distance range (Figure 9c) is more consistent with models with large negative velocity gradients (Figure 17).

[34] The characteristics of the *SH* waves observed at the diffracted distance range (a linearly increasing travel time delay of 10 s across the seismic array; the existence of a triplicated phase; the identical slowness of multiple *ScS* phases to that of the direct waves; the relative timing and amplitude among different phases; and the rapid variations of waveform across the small epicentral distances; Figures 9a and 9b) and the rapid increase of relative *ScS* amplitude from 82° to 95° can be best explained by a 300-km-thick layer with a strong negative velocity gradient from 2% (top) to 10–12% (bottom) and steeply dipping boundaries at the base of the mantle (Figures 9d, 9e, and 9f). The frequency content of the direct arrivals observed in the southern part of the seismic array (Figure 9b) is consistent with a sharp decrease of shear velocity at the top of the boundary layer. The linearly increasing travel time delay of 10 s is also exactly predicted by this sharp decrease of shear velocity at 300 km above the core-mantle boundary (Figures 9d and 9a). We should, however, add a cautionary note that not all the observed waveform features are

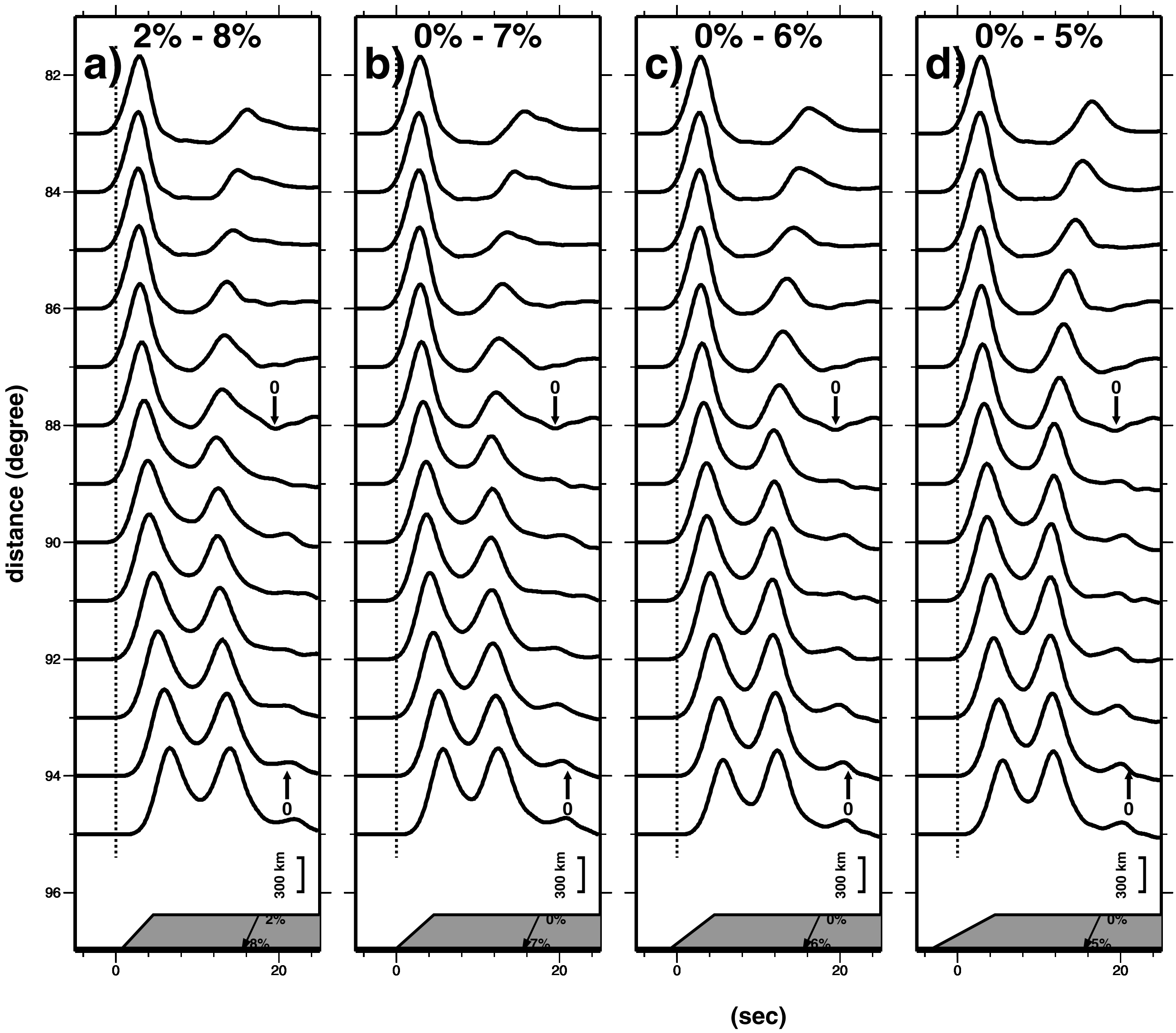

Figure 17. Synthetics at a distance range of 83°–95° calculated using 300-km-thick models with various background negative velocity gradients and geometries. These models predict same differential travel times between *S* and *ScS* phases, indicating that trade-offs exist between the geometry and the magnitude of the velocity gradient in predicting the *ScS-S* separation at this distance range. Note, however, large negative velocity gradients predict a rapid increase of relative *ScS* amplitude from 83° to 95°. There are no lateral velocity gradients within the model wedges. The phase labeled as 0 is a truncation phase in the hybrid method calculation.

explained by our two-dimensional models and three-dimensional effects of wave propagation could be important.

6. Interpretations

[35] The 3% negative velocity gradient beneath the central Pacific at the base of the mantle may reasonably be explained by pure thermal effects of a temperature gradient across a thermal boundary layer. *Wen et al.* [2001] have extensively discussed various proposals for explaining the seismic characteristics observed in the bottom boundary layer beneath the South Atlantic Ocean and their difference with those inferred beneath the central Pacific. The magnitude of the negative velocity gradient, the steeply dipping edges, and the unique presence of the boundary layer beneath the South Atlantic Ocean can be best explained by partial melt driven by a compositional change produced early in the Earth's history and a thermal gradient within the boundary layer [*Wen et al.*, 2001]. We focus here on how partial melt could explain the negative velocity gradient observed within the thermochemical boundary layer and possible thermal conditions which would consistently explain the seismic structures beneath the central Pacific and South Atlantic Oceans.

[36] In the partial melt scenario within a thermochemical boundary layer, melting at a chemical boundary or at the eutectic temperature results in an abrupt decrease of velocity at 300 km above the core-mantle boundary, and an increase of both melt fraction and temperature produces a strong negative velocity gradient toward the core-mantle boundary. We show an example for a hypothetical binary composition system for the case of eutectic partial melting (Figure 18). Mantle composition M intersects eutectic melting temperature at 300 km above the core-mantle boundary and starts to partially melt with a melt fraction $x_1/(x_1 + y_1)$ and a melt composition E. As a result, shear velocity experiences a first-order negative discontinuity at 300 km above the core-mantle boundary. A positive temperature gradient within the boundary layer generates an

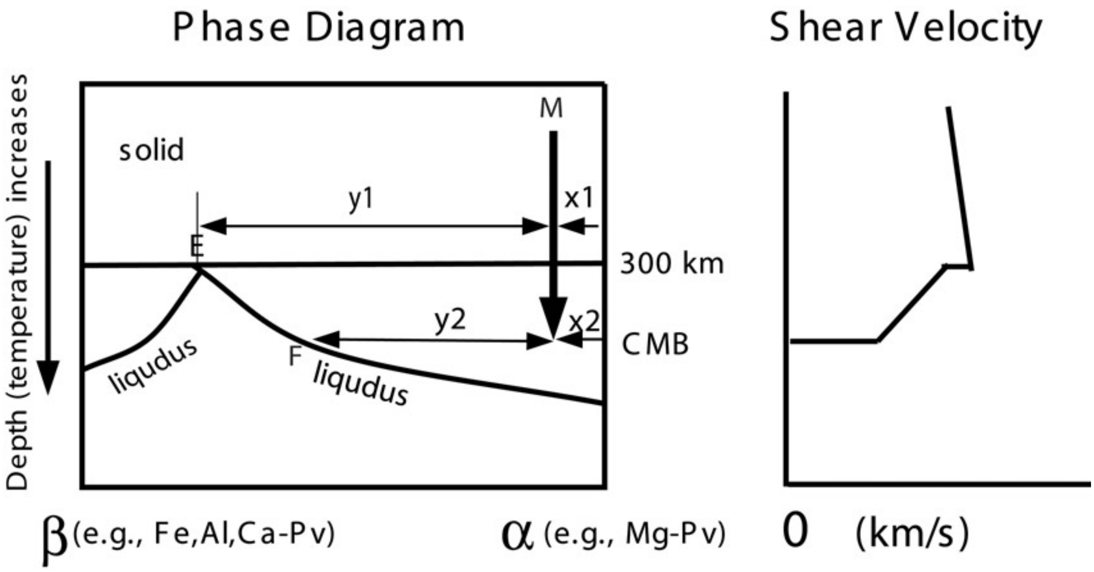

Figure 18. A schematic phase diagram to illustrate a partial melt scenario and its corresponding shear velocities as a function of depth. The composition is assumed to be a simple binary system consisting of a major component α (e.g., Mg-perovskite) and a minor component β (e.g., Fe, Ca Al, or volatile elements enriched).

increase of fraction of the melt from $x_1/(x_1 + y_1)$ to $x_2/(x_2 + y_2)$ and a change of melt composition from E to F. The increase of melt fraction and temperature results in a strong negative velocity gradient toward the core-mantle boundary (Figure 18). In reality, if the composition anomaly has a low partial melting temperature, the depth and velocity of the top of the thermochemical layer would be controlled by the onset of the chemical anomaly rather than the eutectic melting.

[37] Figure 19 illustrates two end-members of possible scenarios which could explain the difference between the seismic structures at the base of the mantle beneath the central Pacific and South Atlantic Oceans. As *Wen et al.* [2001] suggest, the following two

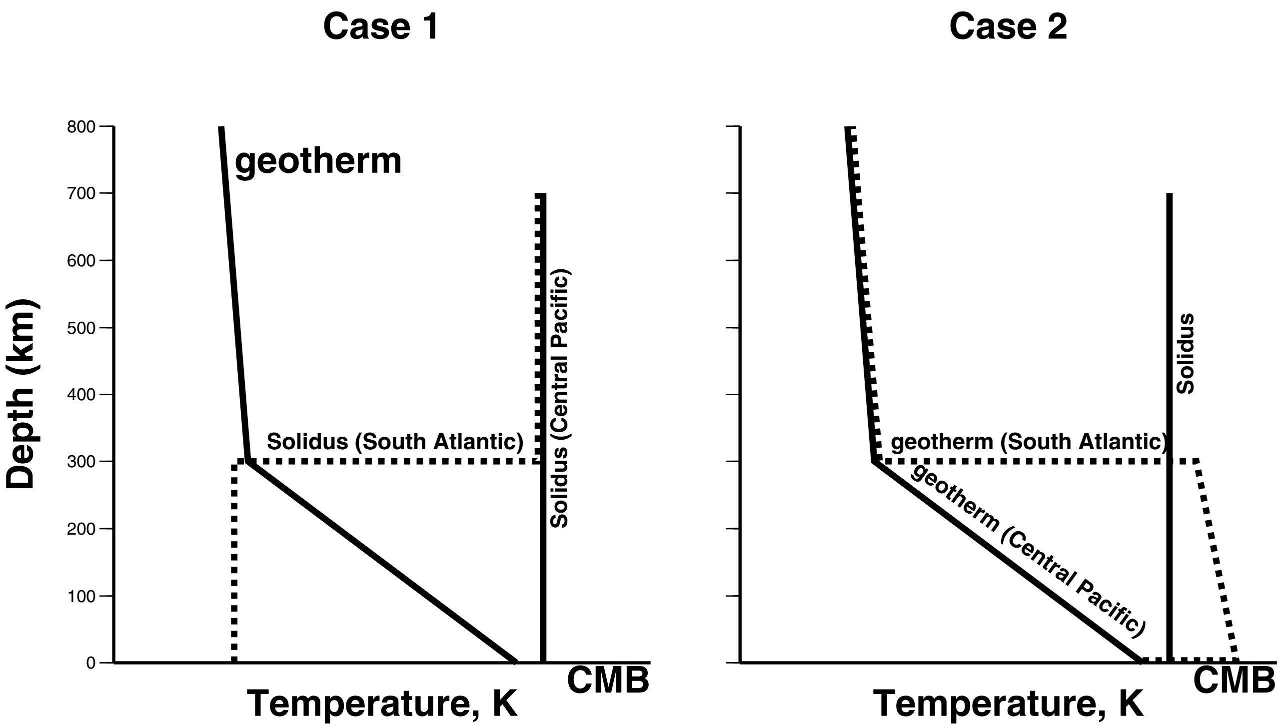

Figure 19. Two end-members of temperature and solidus profiles at the base of mantle beneath the central Pacific and South Atlantic Oceans. In case 1 the South Atlantic Ocean has a same geotherm as the central Pacific, but it has a depressed solidus at the base of the mantle because of the compositional change. In case 2, materials have the same solidus beneath both the central Pacific and South Atlantic Oceans, but the temperatures are locally elevated beneath the South Atlantic Ocean owing to more radiogenic heating.

characteristics of a primordial chemical anomaly should significantly affect its melting behavior:

1. It may be enriched in less compatible elements (e.g., Al, Fe, Ca) and perhaps some volatile components. These elements could significantly depress the melting temperature.

2. It may also be enriched in heat-producing incompatible elements, such as U, Th, and K. Internal temperature may be so elevated owing to radiogenic heating that it sustains the partial melting or remelts locally.

[38] In case 1, both the central Pacific and South Atlantic Oceans have an identical geotherm, with an adiabatic temperature gradient in the mantle followed by a steep thermal gradient in the bottom of the mantle. Mantle materials at the base of the mantle beneath the South Atlantic Ocean have a lower partial melting temperature because of the compositional change (Figure 19, left). In case 2, mantle has a same solidus for materials beneath both the central Pacific and South Atlantic Oceans, but the temperatures are locally elevated at the base of the mantle beneath the South Atlantic Ocean owing to more radiogenic heating (Figure 19, right). In both cases, the temperature at the base of the mantle is below the solidus beneath the central Pacific and is above the solidus beneath the South Atlantic Ocean due to a depressed partial melting temperature and/or an elevated internal temperature there. The bottom thermal gradients produce a 3% negative velocity gradient beneath the central Pacific by pure thermal effects and a 2–10% negative velocity gradient beneath the South Atlantic Ocean as a result of partial melting.

7. Conclusion

[39] An *SH* hybrid method is developed for calculating synthetic seismograms involving two-dimensional localized heterogeneous structures. Hybrid method is a combination of analytic and numerical methods, with the finite difference technique applied in the heterogeneous region only and analytic methods outside. The generalized ray theory solutions from a seismic source are used in the finite difference initiation process. The seismic motions, after interacting with the heterogeneous structures, are propagated back to the Earth's surface analytically with the aid of the Kirchhoff method. Comparisons of synthetics calculated by the hybrid method and the general ray theory yield good agreements.

[40] We collect and present *SH* observations at the distance range of 83°–108° for those sampling the base of the mantle beneath the central Pacific and the South Atlantic Oceans. The observed *SH* waves sampling these two regions of the core-mantle boundary, however, show very different characteristics across the epicentral distance range of 83°–108°. The *SH* waves sampling the core-mantle boundary beneath the central Pacific show a linearly increasing delay of 4 s from 98° to 108° and discernible *ScS* phases up to an epicentral distance of 102°. The *SH* waves propagating through the base of the mantle beneath the South Atlantic Ocean, on the other hand, exhibit a linearly increasing delay of 10 s from 98° to 108°, discernible multiple *ScS* phases with same slowness as the direct *SH* waves up to 108°, and rapid variations of waveform across small epicentral distances. The observations sampling the South Atlantic Ocean at a closer distance range of 83°–95° show large *ScS-S* time separations and a rapid increase of *ScS* amplitude from 83° to 95°.

[41] We apply the hybrid method and study the shear velocity structures and the interaction of *SH* waves with these velocity structures at the base of the mantle. Of particular emphases are the effects of a negative velocity gradient at the base of the mantle and its geometry on the seismic travel times, waveforms, and variations of seismic waveforms cross small epicentral distances. Synthetic tests indicate that while the observations sampling the central Pacific can be explained by a negative shear velocity gradient of 3% (relative to PREM) at the bottom 300 km of the mantle, those sampling the South Atlantic Ocean require a 300-km-thick bottom boundary layer with a larger negative velocity gradient from 2% (top) to 10–12% (bottom) and steeply dipping edges. The observations sampling the core-mantle boundary region beneath the South Atlantic Ocean cannot instead be explained by models with a negative velocity gradient of 3% embedded with ultralow-velocity zones with thicknesses of tens of kilometers. The negative velocity gradient at the base of mantle beneath the South Atlantic Ocean can be best explained by partial melt driven by a compositional change produced in the early Earth's history and a vertical thermal gradient, while that beneath the central Pacific may reasonably be attributed to pure thermal effects within a thermal boundary layer.

Appendix A: Finite Difference Formulations in the Interfaces of Three Defined Regions

[42] We follow the notation of *Virieux* [1984]. For the region where $n = 3$ and $m > 3$,

$$V_{i,j}^{k+1/2} = V_{i,j}^{k-1/2} + L_{i,j}\Big\{\Big(\sum\nolimits_{i+1/2,j}^{k} - \sum\nolimits_{i-1/2,j}^{k}\Big) + \Big[\Big(T_{i,j+1/2}^{k} - T_{i,k}^{0,k}\Big) - T_{i,j-1/2}^{k}\Big]\Big\},$$

$$\sum\nolimits_{i+1/2,j}^{k+1} = \sum\nolimits_{i+1/2,j}^{k} + M_{i+1/2,j}\Big(V_{i+1,j}^{k+1/2} - V_{i,j}^{k+1/2}\Big),$$

$$T_{i,j+1/2}^{k+1} = T_{i,j+1/2}^{k} + M_{i,j+1/2}\Big[V_{i,j+1}^{k+1/2} - \Big(V_{i,j}^{k+1/2} + V_{i,j}^{0,k+1/2}\Big)\Big],$$

where k is the index of time steps, i and j are for x axis and z axis discretizations. $(\Sigma, T) = (\tau_{xy}, \tau_{xz})$, $L = (1/\rho)\ [(dt)/(dx)]$ and $M = \mu\ [(dt)/(dx)]$; dx and dt are space and time discretizations and μ is shear modulus. (V^0, T^0) are solutions for direct incident wave (I_0). Here the relationship $T = I_0 + R$ is used.

[43] For the left boundary, $m = 3$

$$V_{i,j}^{k+1/2} = V_{i,j}^{k-1/2} + L_{i,j}\Big\{\Big[\Big(\sum\nolimits_{i+1/2,j}^{k} - \sum\nolimits_{i+1/2,j}^{0,k}\Big) - \sum\nolimits_{i-1/2,j}^{k}\Big] + \Big(T_{i,j+1/2}^{k} - T_{i,j-1/2}^{k}\Big)\Big\},$$

$$\sum\nolimits_{i+1/2,j}^{k+1} = \sum\nolimits_{i+1/2,j}^{k} + M_{i+1/2,j}\Big[V_{i+1,j}^{k+1/2} - \Big(V_{i,j}^{k+1/2} + V_{i,j}^{0,k+1/2}\Big)\Big],$$

$$T_{i,j+1/2}^{k+1} = T_{i,j+1/2}^{k} + M_{i,j+1/2}\Big(V_{i,j+1}^{k+1/2} - V_{i,j}^{k+1/2}\Big),$$

where (V^0, Σ^0) are solutions for whole wave field (T_0) due to one-dimensional structure for grids $n > 3$ and reflected wave field (R_0) for grids $n < 3$. Here the relationships $S = T - T_0$ and $S = R - R_0$ are used.

[44] **Acknowledgments.** I thank the Kaapvaal Seismic Team for early access to the seismic data and Jascha Polet for assistance in collecting the Trinet data. I also thank Matthew Fouch, an anonymous reviewer, and the Associate Editor for constructive reviews. This work is supported by an NSF grant EAR0001232.

References

Dziewonski, A., and D. L. Anderson, Preliminary reference Earth model, *Phys. Earth Planet. Inter.*, *25*, 297–356, 1981.

Fouch, M. J., P. Silver, and D. E. James, Probing for shear wave anisotropy in the lowermost mantle beneath the Atlantic and Indian Oceans, *Eos Trans. AGU 80*(46), Fall Meet. Suppl., F759, 1999.

Garnero, E. J., S. P. Grand, and D. V. Helmberger, Low *P*-wave velocity at the base of the mantle, *Geophys. Res. Lett.*, *23*, 977–980, 1993.

Helmberger, D. V., Theory and application of synthetic seismograms, in *Earthquakes: Observation, Theory and Interpretation*, edited by H. Kanamori, pp. 173–222, Soc. It. di Fis., Bologna, Italy, 1983.
Helmberger, D. V., L. Wen, and X. Ding, Seismic evidence that the source of Iceland hotspot lies at the core-mantle boundary, *Nature*, *396*, 251–255, 1998.
Helmberger, D. V., S. Ni, L. Wen, and J. Ritsema, Seismic evidence for ultralow-velocity zones beneath Africa and eastern Atlantic, *J. Geophys. Res.*, *105*, 23,865–23,878, 2000.
Lay, T., Q. Williams, and E. J. Garnero, The core-mantle boundary layer and deep Earth dynamics, *Nature*, *392*, 461–468, 1998.
Mori, J., and D. V. Helmberger, Localized boundary layer below the mid-Pacific velocity anomaly identified from *PcP* precursor, *J. Geophys. Res.*, *100*, 20,359–20,365, 1995.
Niu, F., and L. Wen, Strong seismic scatterers near the core-mantle boundary west of Mexico, *Geophys. Res. Lett.*, *28*, 3557–3560, 2001.
Revenaugh, J., and R. Meyer, Seismic evidence of partial melt within a possibly ubiquitous low-velocity layer at the base of the mantle, *Science*, *277*, 670–673, 1997.
Ricard, Y., M. A. Richards, C. Lithgow-Bertelloni, and Y. LeStunff, A geodynamic model of mantle density heterogeneity, *J. Geophys. Res.*, *98*, 21,895–21,909, 1993.
Ritsema, J., E. Garnero, and T. Lay, A strongly negative shear velocity gradient and lateral variability in the lowermost mantle beneath the Pacific, *J. Geophys. Res.*, *102*, 20,395–20,411, 1997.
Stead, R. J., and D. V. Helmberger, Numerical-analytical interfacing in two dimensions with applications to modeling NTS seismograms, *Pure Appl. Geophys.*, *128*, 153–174, 1988.
Vidale, J. E., and M. Hedlin, Evidence for partial melt at the core-mantle boundary north of Tonga from the strong scattering of seismic waves, *Nature*, *391*, 682–684, 1998.
Virieux, J., *SH*-wave propagation in heterogeneous media: Velocity-stress finite-difference method, *Geophysics*, *49*, 1933–1957, 1984.
Wen, L., Intense seismic scattering near the Earth's core-mantle boundary beneath the Comoros hotspot, *Geophys. Res. Lett.*, *27*, 3627–3630, 2000.
Wen, L., and D. L. Anderson, The fate of the slabs inferred from 130 Ma subduction and seismic tomography, *Earth Planet. Sci. Lett.*, *133*, 185–198, 1995.
Wen, L., and D. V. Helmberger, A 2-D *P-SV* hybrid method and its application to modeling localized structures near the core-mantle boundary, *J. Geophys. Res.*, *103*, 17,901–17,918, 1998a.
Wen, L., and D. V. Helmberger, Ultra low velocity zones near the core-mantle boundary from broadband *PKP* precursors, *Science*, *279*, 1701–1703, 1998b.
Wen, L., P. Silver, D. James, and R. Kuehnel, Seismic evidence for a thermo-chemical boundary layer at the base of the Earth's mantle, *Earth Planet. Sci. Lett.*, *189*, 141–153, 2001.
Wysession, M. E., A. Langenhorst, M. J. Fouch, K. M. Fischer, G. I. Al-Eqabi, P. J. Shore, and T. J. Clark, Lateral variations in compressional/shear velocities at the base of the mantle, *Science*, *284*, 120–125, 1999.

L. Wen, Department of Geosciences, State University of New York at Stony Brook, Stony Brook, NY 11794, USA. (Lianxing.Wen@sunysb.edu)